

Accepted Manuscript

The mechanical and microstructural behaviour of calcite-dolomite composites: An experimental investigation

Alexandra Kushnir, L.A. Kennedy, Santanu Misra, Philip Benson, J.C. White



PII: S0191-8141(14)00292-2

DOI: [10.1016/j.jsg.2014.12.006](https://doi.org/10.1016/j.jsg.2014.12.006)

Reference: SG 3171

To appear in: *Journal of Structural Geology*

Received Date: 31 March 2014

Revised Date: 4 December 2014

Accepted Date: 14 December 2014

Please cite this article as: Kushnir, A., Kennedy, L.A., Misra, S., Benson, P., White, J.C., The mechanical and microstructural behaviour of calcite-dolomite composites: An experimental investigation, *Journal of Structural Geology* (2015), doi: 10.1016/j.jsg.2014.12.006.

This is a PDF file of an unedited manuscript that has been accepted for publication. As a service to our customers we are providing this early version of the manuscript. The manuscript will undergo copyediting, typesetting, and review of the resulting proof before it is published in its final form. Please note that during the production process errors may be discovered which could affect the content, and all legal disclaimers that apply to the journal pertain.

1 **The mechanical and microstructural behaviour of calcite-dolomite composites: An**
2 **experimental investigation**

3
4 **Authors:**

5 Kushnir, Alexandra^{a,1,*}

6 Kennedy, L.A.^a

7 Misra, Santanu^{b,2}

8 Benson, Philip^{b,3}

9 White, J.C.^c

10
11 ^aUniversity of British Columbia, Department of Earth, Oceans, and Atmospheric Sciences, 2020-
12 2207 Main Mall, Vancouver, British Columbia, Canada, V6T 1Z4

13
14 ^bGeological Institute, Department of Earth Sciences, Swiss Federal Institute of Technology,
15 Sonneggstrasse 5, Zurich 8092, Switzerland

16
17 ^cUniversity of New Brunswick, Department of Earth Sciences, 2 Bailey Dr., Fredericton, New
18 Brunswick, Canada, E3B 5A3

19
20 Submitted to the Journal of Structural Geology

21
22
23 **Keywords:** calcite, dolomite, experiments, shear strain, high temperature, high pressure, grain
24 boundary sliding, fracture, strain partitioning

25
26 *Corresponding author: Email address: alexandra.kushnir@gmail.com (Alexandra Kushnir)

27

¹ Institut des Sciences de la Terre d'Orléans, UMR 7327 – CNRS/Université d'Orléans, 1A, Rue de la Férollerie, 45071 Orléans Cedex 2, France

² GNS Science, 1 Fairway Drive, Avalon 5010, Wellington, New Zealand

³ Rock Mechanics Laboratory, School of Earth and Environmental Sciences, Burnaby Building, University of Portsmouth, PO1 3QL, United Kingdom

28 **Abstract**

29 The styles and mechanisms of deformation associated with many variably dolomitized
30 limestone shear systems are strongly controlled by strain partitioning between dolomite and
31 calcite. Here, we present experimental results from the deformation of four composite materials
32 designed to address the role of dolomite on the strength of limestone. Composites were
33 synthesized by hot isostatic pressing mixtures of dolomite (Dm) and calcite powders (% Dm:
34 25%-Dm, 35%-Dm, 51%-Dm, and 75%-Dm). In all composites, calcite is finer grained than
35 dolomite. The synthesized materials were deformed in torsion at constant strain rate (3×10^{-4} and
36 $1 \times 10^{-4} \text{ s}^{-1}$), high effective pressure (262 MPa), and high temperature (750°C) to variable finite
37 shear strains. Mechanical data show an increase in yield strength with increasing dolomite
38 content. Composites with <75% dolomite (the remaining being calcite), accommodate
39 significant shear strain at much lower shear stresses than pure dolomite but have significantly
40 higher yield strengths than anticipated for 100% calcite. The microstructure of the fine-grained
41 calcite suggests grain boundary sliding, accommodated by diffusion creep and dislocation glide.
42 At low dolomite concentrations (i.e. 25%), the presence of coarse-grained dolomite in a micritic
43 calcite matrix has a profound effect on the strength of composite materials as dolomite grains
44 inhibit the superplastic flow of calcite aggregates. In high (>50%) dolomite contents samples, the
45 addition of 25% fine-grained calcite significantly weakens dolomite, such that strain can be
46 partially localized along narrow ribbons of fine-grained calcite. Deformation of dolomite grains
47 by Mode I cracks and shear fractures is observed; there is no intracrystalline deformation in
48 dolomite irrespective of its relative abundance and finite shear strain.

49

50 1. Introduction

51 The styles and mechanisms of deformation associated with many variably dolomitized
52 limestone shear systems are strongly controlled by strain partitioning between dolomite and
53 calcite. Furthermore, the mechanical behaviour of shear zones that form in calcite-dolomite
54 composites is likely a function of external parameters (e.g. P_c, P_p, T , and $\dot{\gamma}$), the mineralogy
55 (calcite/dolomite content; (Delle Piane et al., 2009a)), and texture (e.g. grain size and porosity)
56 of the rock. Carbonate fault rocks can have heterogeneous distributions and variable contents of
57 calcite and dolomite. For instance, fluid flow during thrusting can result in partial de-
58 dolomitization (i.e. calcite formation) of carbonates resulting in heterogeneous distribution of
59 calcite and dolomite in fault rocks (Erikson, 1994). Conversely, shear strain, in tandem with fluid
60 flow, may result in a more dolomite-rich fault rock than the protolith due to the dissolution of
61 calcite and subsequent passive enrichment of dolomite along thrust faults (Kennedy and Logan,
62 1997). Fault rocks derived from carbonate rocks can therefore be composed of variable amounts
63 of dolomite and calcite and grain sizes distributions within the fault rocks can be heterogeneous.
64 In many shear zones, dolomite is demonstrably stronger than calcite, but the amount of dolomite
65 required to significantly change the rheological behaviour of carbonate shear zones is poorly
66 understood. Field observations suggest that dolomite may lead to the embrittlement of limestone
67 (Viola et al., 2006). However, despite the common occurrence of limestone-dolomite
68 composites, the influence of dolomite content on the strength of limestone under both ambient
69 and high temperature conditions is poorly understood.

70 The deformation response of pure calcite and, to a lesser extent, pure dolomite under a
71 variety of crustal conditions is well understood. Field observations suggest that under similar
72 conditions of deformation, below amphibolite facies metamorphism, dolomitic rocks are stronger
73 than limestone of similar grain size and porosity. During deformation, dolomite generally
74 becomes highly fractured whereas calcite undergoes dislocation creep and dynamic
75 recrystallization (Bestmann et al., 2000; Erikson, 1994; Woodward et al., 1988). Under similar
76 experimental deformation conditions, dolomite rock is stronger and less ductile than limestone
77 (Davis et al., 2008; Griggs et al., 1951, 1953; Handin and Fairburn, 1955; Higgs and Handin,
78 1959; Holyoke et al., 2013). At high temperatures ($> 700^\circ\text{C}$), coarse grained dolomite is still
79 stronger than calcite; however, fine-grained dolomite rocks (grains less than $15\ \mu\text{m}$ in diameter)
80 weaken significantly and can be weaker than calcite-rich rocks deformed under the same
81 conditions (Davis et al., 2008; Delle Piane et al., 2009a; Delle Piane et al., 2008; Holyoke et al.,
82 2013).

83 In this study, we address the role of coarse-grained dolomite on the strength and
84 microstructural evolution of calcite-dolomite composites. Synthetic, hot isostatically pressed
85 (HIP) calcite-dolomite (Cc-Dm) composites of four unique compositions - 1) 25%Dm:75%Cc,
86 2) 35%Dm:65%Cc, 3) 51%Dm:49%Cc, 4) 75%Dm:25%Cc (hereafter designated by their
87 dolomite content (%): Dm25, Dm35, Dm51, and Dm75) - were deformed in a torsion apparatus
88 at elevated temperature and confining pressure to determine their rheological behaviour and to
89 evaluate the effect of dolomite content and grain size on rock strength. A total of 13 rock
90 deformation experiments were conducted at the following conditions: temperature (T) of 750°,
91 effective pressure (P_{eff}) of 262 MPa, imposed maximum shear strain rates ($\dot{\gamma}$) of $1 \times 10^{-4} \text{ s}^{-1}$ and
92 $3 \times 10^{-4} \text{ s}^{-1}$, and total shear strains (γ) between 0.16 and 5.5. We observe that 1) in carbonate
93 composites, even low dolomite contents greatly affect rock strength; 2) coarse-grained dolomite
94 accommodates strain by brittle deformation in high dolomite content samples; and 3) calcite
95 deforms by dislocation glide and diffusion creep assisted grain boundary sliding. Finally, we
96 compare the experimental results to other studies and comment on their application to natural
97 deformation environments.

98

99 2. Starting Material

100 2.1. Starting Powders and Sample Preparation

101 Two end member powders (coarse-grained dolomite and fine-grained calcite; described
102 below) were mixed in varying proportions to produce four distinct compositions: Dm25, Dm35,
103 Dm51, and Dm75.

104 Reagent-grade calcite powder (Minema 1™) was supplied by Alberto Luisoni AG,
105 Mineral- & Kunststoffe and is characterized by equiaxed calcite grains exhibiting rare growth
106 twins. The powder has a modal grain size of 9 μm (Figure 1A), as measured with a Mastersizer
107 2000 laser diffraction particle size analyser (Malvern Instruments Ltd.). Rietveld refinement of
108 XRD spectra (Raudsepp et al., 1999) of the calcite powder confirms its composition to be 99%
109 CaCO_3 ; the remaining constituents are Mg, Al, Fe, and Si oxides.

110 A 4 kg block of Badshot marble, a natural dolomite marble from the Selkirk Mountains
111 of British Columbia, was crushed to produce a powder with a broad grain size distribution and
112 modal grain size of $\sim 120 \mu\text{m}$ (Figure 1A). Badshot dolomite is characterized by coarse dolomite
113 grains (mean grain size of 477 μm , Austin and Kennedy (2005)) featuring lobate grain
114 boundaries and fine, polygonal grains. Cleavage and twinning are prevalent in most grains

115 (Austin, 2003; Austin and Kennedy, 2005; Austin et al., 2005). XRD analysis of the powder
116 indicates a mineralogy that is ~99.8% dolomite. Thin section analysis reveals trace quantities
117 (<< 1%) of pyrite, apatite, calcite, tremolite, and white mica; these accessory phases are
118 sufficiently low in abundance to be undetected by XRD analysis.

119 The powder mixtures were mechanically shaken to create homogeneous mixtures;
120 the grain size distributions of the mixed powders are shown in Figure 1B. The starting powders
121 have a bimodal grain size distribution, reflecting the dolomite proportion. The powder mixtures
122 were then dried at 120°C for a minimum of 24 hours before being cold pressed into stainless
123 steel, cylindrical canisters. The canisters were filled and pressed in 20g increments to produce
124 homogenous packing of the powder along the canister length. This was done to avoid pressure
125 shadow development during heat treatment. Pressing was done with an Enerpac-H-Frame 50 ton
126 press up to a load of 40 tons, corresponding to a vertical stress of 200 MPa. A small volume of
127 alumina powder with a porosity of ~30% was placed at the top and bottom of the canisters to act
128 as a CO₂ sink for decarbonating dolomite. This ensured the migration of the emitted CO₂ to the
129 storage areas, allowing the porosity to remain reduced in the rest of the canister.

130 All canisters were welded shut and, subsequently, hot isostatic pressed (HIP) to produce
131 synthetic composite rock samples. The HIP was performed in a large volume, internally heated,
132 argon gas apparatus at ETH-Zürich under a confining pressure of 170 MPa (Delle Piane et al.,
133 2009a) and a temperature of 700°C for 4 hours. The resulting products form a suite of coherent,
134 sintered material of known compositions and consistent grain size. Rietveld refinements of XRD
135 spectra collected on the composite samples did not detect periclase (MgO) nor lime (CaO),
136 indicating that there was no detectable decarbonation of dolomite or calcite during the HIP
137 process. Rietveld refinements also confirm the four starting material compositions as containing
138 25%, 35%, 51%, and 75% dolomite.

139 2.2. *Microstructural and Textural Analyses*

140 Starting materials were thin sectioned normal to the canister long axes (i.e. normal to the
141 pressing direction) and polished using a rotary polishing wheel and 200 nm silica bead colloidal
142 solution. Backscatter electron (BSE) and secondary electron (SE) SEM images were collected
143 using a thermal field emission type Zeiss Sigma SEM (UBC) with 1.3 nm resolution at 20 kV
144 acceleration voltage. Probe current was 1.37 nA.

145 Electron Backscatter Diffraction (EBSD) analysis was completed to map the
146 crystallographic preferred orientation (CPO) of the starting materials and the evolution of the

147 CPO of subsequently deformed materials. EBSD measurements were made using an EDAX
 148 DigiView EBSD camera (UBC). Samples were inclined to the electron beam at 70° to produce
 149 clear diffraction patterns for automated identification using Orientation Imaging Microscopy
 150 (OIM™) Data Collection and Data Analysis software. The average crystallographic orientation
 151 for each individual grain was used to generate pole figures using PF_Euler_PC.exe (Pera et al.,
 152 2003). CPO strength is characterized by the J-texture index (the density distribution of the
 153 crystallographic orientations (Miyazaki et al., 2013)); we use both the pole figure J-index (pfJ)
 154 and the J-index (J). Indices vary from 1 (random crystallographic orientations; no CPO) to
 155 infinity (one discrete crystallographic orientation). The J-index (calculated using mtex-3.5.0
 156 (Bachmann F., 2010)) incorporates all slip systems, while the pfJ-index (calculated using
 157 PF_Euler_PC.exe) is a measure of the strength of the CPO along a defined slip axis (i.e. c-axis).

158 Energy-dispersive X-ray spectroscopy (EDS) was performed on all analyzed samples
 159 using an Apollo XL Silicon Drift Detector (SDD) at a typical working distance of 14 mm. EDS
 160 data were collected in conjunction with EBSD diffraction patterns and used to identify dolomite
 161 based on the apparent relative concentrations of Mg:Ca. EDS spectra suggesting Ca:Mg ratios ~ 1
 162 were interpreted as indicating the presence of dolomite.

163 2.3. Starting Material Characterization

164 The skeletal and isolated pore space volume, V_{s+i} , of each sample was determined prior to
 165 deformation using a Micromeritics Multivolume Pycnometer 1305 helium pycnometer.
 166 Connected porosity, ϕ , was calculated from the geometric bulk volume, V_b , and skeletal and
 167 isolated pore volume:

$$168 \quad \phi = \left(1 - \frac{V_{s+i}}{V_b}\right) \times 100\% \quad (1)$$

169 The final composition, porosity, and density of the starting materials are given in Table 1.

170 Calcite grains are approximately equiaxed, generally have straight grain boundaries, and
 171 are closely packed with triple junction grain boundaries (Figure 2A and 2C). Porosity is isolated
 172 along grain boundaries and at triple junctions and therefore may not be accessed by the helium
 173 gas pycnometer; the porosity data obtained by pycnometry are considered lower limits.

174 Dolomite grains are generally distributed homogeneously in all synthetic starting
 175 materials (Figures 2B and 2D); rarely, coarser grains of dolomite may cluster together. Dolomite
 176 grains are angular to subangular and contain intragranular fractures; straight fractures appear to
 177 follow cleavage planes but curved fractures also exist. Since these fractures do not continue into

178 the calcite matrix, they are attributed to the crushing process used to produce the starting
179 dolomite powder. Intergranular porosity is greatest at dolomite-calcite interfaces (Figure 2C).

180 Observations of the Dm25 and Dm35 starting materials made by SEM reveal randomly
181 distributed circular concentrations of calcite up to ~500 μm in diameter (Figure 3A). These
182 concentrations are spherical and likely accreted during mechanical shaking of the starting
183 powders. The margins of these calcite aggregates are accentuated by concentrations of edge-
184 parallel oriented dolomite grains (Figure 3B). Similarly, coarse dolomite grains can also be
185 encased in a halo of predominantly fine-grained calcite.

186 Individual calcite grains within the starting materials are undeformed, showing little to no
187 undulose extinction. Lower hemisphere stereographic projections for calcite obtained from
188 EBSD analysis indicate a weak CPO of the calcite c-axis (Figure 2B and 2D). The c-axis is
189 oriented perpendicular to the load direction during cold pressing as observed by Rutter et al.
190 (1994b), and regardless of calcite content does not vary significantly. Dolomite in the starting
191 materials shows no CPO along any of the common dolomite glide planes (Figures 2B and 2D).
192 The CPO peaks on the dolomite stereonet are artefacts caused by the relatively small number of
193 dolomite grains in the scanned area (a result of their large grain size) and cause erroneously high
194 pfJ-indices, indicating strong textures focused around single grains.

195 Grain size distributions based on two-dimensional images for Dm25 and Dm75 were
196 calculated using Orientation Imaging Microscopy (OIMTM) data analysis software by fitting a
197 model ellipse to each crystallographically identified grain (Figure 4). Both starting compositions
198 show similar calcite grain size distributions; Dm25 and Dm75 have modal calcite grain sizes of
199 5.5 μm and 4.5 μm , respectively (Figure 4A). Dolomite grain size distributions are shown in
200 Figure 4B. These estimates are less precise than for calcite because there are fewer dolomite
201 grains in the scan areas, but we observe a broad grain size distribution ranging between 0 and
202 100 μm .

203

204 **3.0. Deformation Apparatus and Techniques**

205 The HIP material was cored into 10 mm and 15 mm diameter cylinders. The core ends
206 were flattened and polished perpendicular to the cylinder sides. Samples were dried in an oven at
207 100°C then mounted between alumina and partially stabilized zirconia spacers and encased in
208 iron jacketing. A jacket thickness of 0.25 mm was used for 15 mm diameter samples. Jackets for

209 10 mm diameter samples were swaged to the correct inner diameter resulting in thickening of the
210 jacket wall to 0.4 mm.

211 All experiments were performed using an internally heated, argon-confining medium
212 pressure vessel equipped with torsion actuator, described by Paterson and Olgaard (2000)
213 (Figure 5A). The experiments were performed in torsion at constant angular displacement rates,
214 corresponding to constant maximum shear strain rates of $1 \times 10^{-4} \text{ s}^{-1}$ and $3 \times 10^{-4} \text{ s}^{-1}$. Confining
215 pressure and temperature were held constant at 300 MPa and 750°C , respectively. Sample
216 temperature was monitored using a K-type thermocouple placed 3mm above the sample. The
217 thermal profile along the sample was calibrated to be consistent within 1°C . All samples were
218 heated and cooled at $10^\circ\text{C}/\text{min}$.

219 The applied torque was measured using an internal load cell equipped with a pair of pre-
220 calibrated linear variable differential transformers (LVDTs). Measured torque was corrected for
221 the strength of the iron jacket (Barnhoorn, 2003) and converted to shear stress at the sample
222 surface:

$$223 \quad \tau = \frac{4\left(3+\frac{1}{n}\right)M}{\pi d^3} \quad (2)$$

224 where τ is shear stress, M is internal torque, d is the diameter of the sample, and n is the stress
225 exponent (Paterson and Olgaard, 2000). In this study, the power law creep relationship used is:

$$226 \quad \dot{\gamma} = A\tau^n e^{\frac{-Q}{RT}} \quad (3)$$

227 where A and Q are constants, n is the stress exponent, T is the temperature, and R is the gas
228 constant (Paterson and Olgaard, 2000). n is experimentally determined for a given composition
229 by conducting a strain rate stepping experiment and plotting the total torque response (M) to
230 changing strain rate ($\dot{\gamma}$). As M is linearly related to τ , the slope of the log-log plot $\dot{\gamma}$ vs. M yields
231 n according to:

$$232 \quad n = \frac{d \ln \dot{\gamma}}{d \ln M} \quad (4)$$

233 Comparison between torsion and axial experiments is necessary for comparing our data to
234 studies of other carbonate systems. At the same nominal strain rates ($\dot{\epsilon} = \dot{\gamma}$), differential stress
235 ($\sigma_1 - \sigma_3$) is calculated:

$$236 \quad \sigma_1 - \sigma_3 = 3^{\frac{1+n}{2n}} \tau \quad (5)$$

237 where σ_1 is the calculated maximum compressive stress, σ_3 is the minimum compressive stress,
238 and τ is shear stress (Paterson and Olgaard, 2000).

239

240 4.0. Mechanical Results

241 To maintain the stability of dolomite, we performed all experiments under unvented
242 conditions and within the stability field of calcite and dolomite (Goldsmith, 1959). XRD analysis
243 revealed no evidence of decarbonation products; we conclude that the low porosity of our
244 starting materials allowed equilibrium pore pressures to be reached by the dissociation of trace
245 amounts of dolomite (Davis et al., 2008; Delle Piane et al., 2009a; Holyoke et al., 2013). We
246 have accounted for the effective pressure caused by the decarbonation of trace amounts of
247 dolomite, such that $P_{\text{eff}}=P_C-P_{\text{CO}_2}$.

248 All experiments performed in this study, including experimental conditions and sample
249 compositions, are summarized in Table 2. Dm25, Dm35, and Dm75 samples were deformed in
250 strain rate stepping experiments to empirically determine the stress exponent n (see Table 2,
251 Figure 6). All mechanical data are fit using Eq. (2) and are shown in Figure 7A (high strain rate
252 experiments) and Figure 7B (low strain rate experiments). High strain rate ($\dot{\gamma} = 3 \times 10^{-4} \text{ s}^{-1}$)
253 experiments were conducted for all four compositions (experiments P1522, P1524, P1525,
254 P1527, P1528, P1537, and P1538) at $T=750^\circ\text{C}$ and $P_c=300 \text{ MPa}$. The shear strain for these
255 experiments exceeded $\gamma = 5$ (Figure 7A). Experiment P1537's (Dm51) heating history is not
256 confidently known beyond $\gamma \sim 2$; only the mechanical data up until this point is used and this
257 sample was not used for microstructural analysis. Low strain rate ($\dot{\gamma} = 1 \times 10^{-4} \text{ s}^{-1}$)
258 experiments were conducted for compositions Dm35 (P1543), Dm51 (P1523), and Dm75
259 (P1533) at $T=750^\circ\text{C}$ and $P_c=300 \text{ MPa}$ (Figure 7B). The maximum shear strain for these
260 experiments was approximately $\gamma \sim 2$.

261 Yield and peak strength of the synthetic composite samples increases with increasing
262 dolomite content (Table 2; Figure 7C). Yield strength was taken as the departure from the elastic
263 response of the material. Experiments P1527 (Dm25) and P1524 (Dm35) are mechanically
264 similar, both reaching a peak strength of $\sim 80 \text{ MPa}$ (Figure 7A). Mechanical steady-state (~ 79
265 MPa) is established in both samples at $\gamma < 0.1$ followed by limited strain hardening in Dm25 at γ
266 ~ 3.75 (Figure 7A). Experiments P1525 and P1528 (Figure 7A) failed due to jacket ruptures
267 resulting from the inherent strength of the Dm51 and Dm75 materials at 15 mm sample
268 diameters. To mitigate this behaviour, Dm51 (P1537) and Dm75 (P1538) sample diameters were
269 reduced to 10 mm so that these compositions could be deformed to high strain. P1537 (Dm51)
270 reached a tenuous steady-state at $\tau \sim 140 \text{ MPa}$ and $\gamma \sim 0.4$ (Figure 7A). The mechanical behaviour
271 of the Dm75 sample evolves throughout deformation: after attaining a peak strength of ~ 178

272 MPa, dramatic strain weakening at $\gamma \sim 1$ is recorded (Figure 7A). Strain hardening and
 273 subsequent strain weakening are observed between $3 < \gamma < 4$. Experiments P1533 and P1543
 274 were halted manually.

275 **5. Microstructure and Texture of Deformed Materials**

276 *5.1 Analytical Methods*

277 After deformation, all samples were cut along the longitudinal tangential section of the
 278 core (Figure 5B) and doubly-polished petrographic thin sections were prepared with
 279 Crystalbond© adhesive. This plane shows the maximum shear strain attained in the sample.

280 In addition to SEM, EBSD, and EDS analyses (see Section 2.2.), microstructures for
 281 transmission electron microscopy (TEM) were selected. After having been mounted on 3mm
 282 copper discs, the areas were thinned by Ar-ion bombardment in a Gatan PIPS thinning unit.
 283 TEM examination was performed with a JEOL 2011 STEM apparatus operated at 200kV.

284 Electron-probe micro-analyses of selected deformed samples were done to confirm exact
 285 grain composition. Data were collected on a CAMECA SX-50 instrument, operating in the
 286 wavelength-dispersion mode using: excitation voltage: 15 kV; beam current: 10 nA; peak count
 287 time: 20 s; background count-time: 10 s; spot diameter: 10 μm . Data reduction was done using
 288 the 'PAP' $\phi(\rho Z)$ method (Pouchou and Pichoir, 1985).

289 *5.2 Microstructure: low dolomite content samples*

290 The circular calcite aggregates identified in starting materials Dm25 and Dm35 (Figure
 291 3) are deformed non-coaxially into thin bands (ellipsoids) of pure calcite with aspect ratios
 292 ranging from 19 to 23 (Figure 8A). These thin layers of pure calcite, interlaced with the calcite-
 293 dolomite mixture, define a compositional layering in the low dolomite content samples (Dm25
 294 and Dm35; Figures 8A and 8B). As these aggregates were originally circular in cross-section and
 295 assuming there was no loss of volume during deformation, the shear strain by simple shear can
 296 be calculated:

$$297 \quad \gamma = \cot \alpha' - \cot \alpha \quad (6)$$

298 where α is the initial angle between a line and the direction of shear, and α' is the same angle
 299 after deformation. For the torsional simple shear assumption, the instantaneous stretching axis is
 300 oriented in the xz -plane at 45° to the direction of shear and is equal to α for the initially circular
 301 aggregates. Accumulation of strain with increasing imposed sample twist produces the maximum

302 stretching direction preserved by the long axis of the elliptical calcite aggregates. The angle
303 between this orientation and the direction of shear is α' (Figure 8A). These features record shear
304 strains of 5.14 and 6.11 for Dm25 and Dm35, respectively.

305 Calcite layers are sheared and rotated nearly parallel to the shear direction, while the
306 surrounding dolomite-calcite mixture defines a shape foliation oblique to the shear direction
307 (Figure 8B), defining a global s-c mylonite fabric. Dolomite grains with high aspect ratios (i.e.
308 aspect ratios > 1) are subject to rigid body rotation and their long axes are aligned subparallel to
309 the layering, inclined to the shear direction; these are interpreted as shape (s-) fabrics (Figures
310 8B and 8C). Accessory pyrite is elongated and passively marks the local fabric (Figure 8C) while
311 thin, discontinuous zones of relative high shear strain are oriented nearly parallel to the shear
312 direction and are interpreted as c-surfaces (Figure 8D).

313 Calcite grains are generally polygonal, equiaxed to tabular, and closely packed with
314 straight grain boundaries meeting at triple junctions (Figure 8E). The more tabular shaped calcite
315 grains are aligned parallel to the shape foliation (inclined to the shear direction; Figure 8E).
316 Calcite grains comprising the pure calcite layers are also mostly equiaxed, with straight grain
317 boundaries exhibiting triple junctions. Two dimensional grain size distributions for Dm25 show
318 possible calcite grain growth during deformation from 6 μm to 7.5 μm (Figure 4A). The
319 dolomite grains show little to no evidence of internal strain nor is there any evidence of grain
320 size reduction due to fracture (Figures 8A and 8C). Dolomite grains do not appear to have
321 sustained any additional fracture (e.g. microcracking and shear fracturing), as fracture density is
322 qualitatively the same as in the starting material. Rounding of dolomite grains less than
323 approximately 50 μm in diameter is observed in all dolomite-poor deformed samples. While
324 dolomite grains $< 100 \mu\text{m}$ show some rounding (Figure 8B and 8E), there is no significant
325 rounding of grains above $\sim 100 \mu\text{m}$.

326 Porosity is visibly reduced with respect to the starting material and is typically preserved
327 at triple junctions of calcite grains (Figure 8E). Locally, there are regions of higher porosity
328 within the calcite matrix aligned along foliation (Figure 8F). These regions are located in
329 pressure shadow-like geometries along the peripheries of some dolomite grains that are $> 70 \mu\text{m}$
330 in diameter (Figure 8F).

331

332 *5.3 Microstructure: High dolomite content samples*

333 In high dolomite content ($> 50\%$) samples, a poorly developed compositional layering is
334 defined by crude variations in grain size and fine-grained, high aspect ratio dolomite (Figure 9A

335 and 9B). Locally, a shape fabric inclined to the shear direction is defined by rotated dolomite
336 grains $<20\ \mu\text{m}$ in diameter (Figure 9B). Areas of localized strain in the patchy calcite layers are
337 common. Thin, interconnected networks of fine-grained calcite form ribbons that define a
338 discontinuous and irregular foliation that is deflected around more rigid coarse-grained dolomite
339 (Figure 9A and 9C). Sheared pyrite grains wrap around dolomite grains (Figure 9A and C).

340 The calcite microstructure is similar to the low dolomite samples; calcite grains are
341 locally equiaxed to tabular, bounded by straight grain boundaries, and form triple junctions with
342 neighbouring calcite grains (Figure 9B). In areas of high dolomite content, irrespective of the
343 overall shape fabric, calcite grain are oriented parallel to the dolomite grain boundaries
344 (especially in narrow regions between dolomite grains; Figure 9B). Two dimensional grain size
345 distributions for P1538 (Dm75) show possible calcite grain size reduction during deformation
346 (from 4.5 to $3.5\ \mu\text{m}$) in Dm75 (Figure 4A).

347 Brittle deformation of dolomite is evident in all high dolomite content samples:
348 intragranular Mode I fractures are common in the larger dolomite grains and are lined with fine
349 grained calcite (Figure 9A). These fractures do not propagate into the surrounding calcite matrix.
350 Locally, dolomite is fragmented by domino-style and antithetic shear fractures (Figure 9A and
351 9D).

352 *5.4 Deformation Textures*

353 EBSD analyses of samples Dm25, Dm35, and Dm75 taken to high strain show a strong
354 crystallographic preferred orientation of calcite crystals (Figure 10). The c-axes define double
355 maxima with the bisecting line normal to the direction of maximum stretching, indicating basal
356 slip activation. With increasing dolomite content, the c-axis CPOs become more diffuse, though
357 pfJ- and J-indices are comparable (Figure 10B vs. 10E). In all cases, the c-axis patterns are most
358 pronounced, followed by the a-axis system. As in the c-axis system, the a-axis girdles are well
359 defined but are symmetric about the direction of shear. While a dominant CPO is observed,
360 calcite grains appear internally strain free, showing little to no evidence for significant internal
361 strain (indicated in the EBSD maps by uniform grain crystal lattices). However, preliminary
362 TEM observations (Figures 11A and 11B) show that, despite the EBSD observations,
363 dislocations are common while subgrains are absent.

364 The spherical calcite aggregates (observed in the starting material, Figure 3) that
365 deformed to ellipses during shear (Figure 8A) have the strongest crystallographic preferred
366 orientations. Figure 12 is a compilation of four EBSD scans across a sheared calcite layer from

367 the dolomite-calcite matrix into the calcite layer. It highlights the effect of the second phase
368 (dolomite) on calcite fabric development. The calcite layer has higher pfJ- and J-indices (Figure
369 12E), indicating a stronger texture than the surrounding calcite-dolomite matrix (Figure 12B,
370 12C, and 12C). The CPO of a region scanned ~600 μm away from the calcite layer (Figure 12C)
371 shows the 'background' CPO of the matrix: both the c and a axes are well defined and
372 asymmetrically distributed around the SZB and normal to the SZB, respectively. Adjacent to the
373 calcite layer (~100 μm away from the calcite band; Figure 12D), which still contains dolomite
374 grains, calcite has a similar CPO to that shown in Figure 12C. Within the calcite layer (Figure
375 12E), the CPOs show the tightest clusters. The c-axis is symmetrically distributed perpendicular
376 to the shear zone boundary (SZB).

377 To illustrate the evolution of fabric with increasing shear strain, thin sections were cut
378 from different longitudinal axial sections (see Figure 5B) from the same core for each
379 experiment, and CPOs were measured using EBSD (Figure 13). The calcite c-axes are inclined
380 to the shear zone boundary and define tighter maxima with increasing shear strain. The pfJ- and
381 J-indices also increase with increasing strain. For the Dm75 experiment, the c-axis maxima are
382 more diffuse than for the Dm25 and Dm35 experiments.

383 There is no well-developed CPO in dolomite from deformed samples (Figure 10C and
384 10F), nor is there pervasive undulose extinction, though Dm75 shows minor undulose extinction
385 in coarse-grained dolomite. The pfJ- and J-indices do not vary significantly from the starting
386 material, although they are higher than the same indices for calcite. We interpret this to be, in
387 large part, due to the limited number of data points used to calculate these values.

388

389 6. Chemical Changes Attending Deformation

390 EDS analysis of calcite and dolomite grains in deformed samples highlights changes in
391 composition with increasing shear strain. In particular, the magnesium contents of calcite grains
392 increase with increasing strain. This is most pronounced in calcite grains proximal to fine-
393 grained dolomite phases. Figure 14 demonstrates the evolution of magnesium transfer from $\gamma=0$
394 (Figure 14A) to the largest strains (Figure 14C) for P1527 (Dm25). At $\gamma=0$, magnesium is
395 restricted to dolomite grains, but with increasing strain magnesium becomes more mobile and
396 defines a foliation between dolomite grains (white streaks in Figure 14C).

397 Electron microprobe analysis was used to quantify the extent of Mg^{2+} migration from
398 dolomite to calcite during deformation in high strain experiments P1527 (Dm25) and P1538

399 (Dm75). Microprobe analysis confirms depletion of Mg^{2+} in fine-grained dolomite proximal to
400 Mg^{2+} enriched calcite in Dm25; however, calcite removed from dolomite grain boundaries is not
401 enriched. Mg-enrichment of calcite is pervasive in Dm75, regardless of proximity to thin ribbons
402 of plastically deformed calcite, owing to the abundance of dolomite throughout the system.
403 Microprobe data can be found in the Supplementary Materials.

404 **7. Discussion**

405 *7.1. The Role of Dolomite*

406 In all our experiments, peak shear stress is higher than that determined for 100% calcite
407 of the same grain size and deformed under similar experimental conditions (Figure 7C). For
408 example, the peak shear stress for pure, synthetic calcite aggregates with an average grain size of
409 $7\ \mu\text{m}$ deformed in torsion at 727°C , $P_c = 300\ \text{MPa}$, and $\dot{\gamma} = 3 \times 10^{-4}\ \text{s}^{-1}$ is 15 MPa (Barnhoorn et
410 al., 2005a). Peak shear stresses for Solnhofen limestone (grain size $\sim 5\ \mu\text{m}$) under the same
411 conditions were $\sim 40\ \text{MPa}$ (Barnhoorn et al., 2005a). Predicted equivalent shear flow stresses for
412 diffusion creep in Mg-rich calcite (Herwegh et al., 2003) and pure calcite (Walker et al., 1990)
413 are 6 MPa and 13 MPa, respectively (see Herwegh et al. (2005) for flow law parameters used).
414 All these peak stresses are significantly lower than the peak shear stress attained during the
415 Dm25 dolomite content experiments (79 MPa for P1522 and 82 MPa for P1527) in this study.
416 These larger recorded shear stresses may be symptomatic of an increased strain rate in the calcite
417 phase as it deforms around rigid dolomite. Indeed, assuming all deformation in our samples is
418 accommodated within the calcite phase, the predicted shear strain rates calculated using the peak
419 shear stresses recorded for P1527 (Dm25) are over one order of magnitude faster ($6 \times 10^{-3}\ \text{s}^{-1}$ and
420 $4 \times 10^{-3}\ \text{s}^{-1}$ for pure and Mg-rich calcite, respectively; see Herwegh et al. (2005) for flow laws and
421 flow law parameters used) than the imposed strain rate of $3 \times 10^{-4}\ \text{s}^{-1}$.

422 In our low-dolomite content experiments (Dm25 and Dm35), coarse-grained dolomite
423 grains show no evidence of extensive brittle or intracrystalline deformation. However, finer
424 grained dolomite ($< 50\ \mu\text{m}$) with aspect ratios > 1 are rotated into the foliation, suggesting their
425 active role as rotating rigid bodies. We propose that most shear strain was partitioned into the
426 fine-grained calcite layers and that although the dolomite grains are not internally strained or
427 highly fractured, the distribution of these rigid bodies acts to create anastomosing, connected
428 networks of calcite grains. In effect, the dispersed dolomite grains provide local resistance to
429 grain boundary sliding and this resistance results in an increase in the flow stresses necessary for
430 steady state deformation.

431 Although we observe a moderate increase in strength in the 51% dolomite experiment
432 relative to Dm25 and Dm35 (Figure 7A), the Dm75 sample shows a two-fold increase in strength
433 over compositions Dm25 (P1522 and P1527) and Dm35 (P1524). We interpret the high yield
434 stress of Dm75 as a result of the load being supported by dolomite-dolomite contacts. We
435 propose that the significant shear stress drop in experiment P1538 (Dm75) represents fracture of
436 dolomite grains by Mode I, shear fractures, and subsequent grain size reduction (refer to Figures
437 9A and 9D). A short-lived steady state is attained once a temporary grain boundary network is
438 established within the fine-grained calcite (Figure 9C), permitting grain boundary sliding. In
439 essence, disruption of the calcite network leads to strain hardening while re-establishment of the
440 calcite networks leads to the final strain weakening (Figure 7A). Similar behaviour is suggested
441 for the strong phases in other multi-phase systems (e.g. Rybacki et al. (2003)). For instance, in
442 quartz-calcite composites, the addition of quartz (the strong phase, analogous to dolomite in our
443 system) significantly increases the flow stress needed for steady state deformation (Rybacki et
444 al., 2003).

445 In our experiments, the high dolomite content (75%) samples are strongest, yet they are
446 significantly weaker than 100% coarse-grained dolomite deformed under similar elevated
447 pressure-temperature conditions (Figure 7C; (Davis et al., 2008; Holyoke et al., 2013). The peak
448 shear stress of 167 MPa achieved in experiment P1538 (Dm75) is lower than the reported
449 strengths for Madoc dolomite (grain size of 240 μm) at 700°C (equivalent yield shear stress of
450 241 MPa; equivalent shear stress at 5% strain of 377 MPa; equivalent $\dot{\gamma} = 2 \times 10^{-4} \text{ s}^{-1}$) and 800°C
451 (equivalent peak shear stress of 257 MPa for an equivalent $\dot{\gamma} = 1.7 \times 10^{-5} \text{ s}^{-1}$). We attribute the
452 relative weakness in our Dm75 sample to the role of calcite networks in weakening the rocks.
453 Coarse-grained dolomite does not undergo any significant intracrystalline plasticity and deforms,
454 instead, by fracture. We interpret that shear strain is partitioned into thin, fine-grained,
455 interconnected calcite-dolomite layers that are developed during shear strain and are deflected
456 around large dolomite clasts (Figure 9C). This shear strain-induced configuration results in a
457 weaker rock.

458 Our data suggest that for dolomite contents below a minimum of 35%, dolomite does not
459 actively deform, but its presence is rate-controlling given the strength of the composites
460 compared to micritic limestone (Figures 7C and 15A). Only when dolomite, the 'strong' phase,
461 is present in sufficient quantities (>51%) to inhibit the flow of calcite and/or restrict calcite flow
462 to narrow, localized bands does brittle fracture of dolomite grains become mechanically

463 significant in accommodating strain, indeed, leading to the initial embrittlement within the
464 system.

465 We propose that in shear systems containing <75% dolomite (with the remaining being
466 calcite), rocks will have the ability to accommodate significant shear strain at much lower shear
467 stresses than dolomite. Conversely, even at low concentrations (i.e. 25%), the presence of
468 coarse-grained dolomite in a micritic calcite matrix will have a profound effect on the strength of
469 composite materials; the strength increases with respect to a pure calcite system since dolomite
470 grains inhibit the superplastic flow of calcite. Eventual embrittlement of dolomite within the
471 system may be required to re-establish plastic networks of fine-grained calcite.

472

473 *7.2 The Case for Grain Boundary Sliding*

474 Contrasting stress exponents determined from the strain rate stepping experiments of
475 Dm25, Dm35, and Dm75 suggest the influence of more than one deformation mechanism. For
476 the adopted relationship, $\dot{\gamma} \propto \tau^n$, calcite-rich samples give $n = 1.7 \pm 0.23$ (Dm35; P1529) and
477 2.0 ± 0.43 (Dm25; P1711), while dolomite-rich samples give $n = 3.6 \pm 0.12$ (Dm75; P1713).
478 Broadly interpreted, a $n \geq 3$ reflects dislocation creep related flow (Weertman, 1957), while
479 $1 < n < 3$ correlates with a grain-size-sensitive (GSS) rheology (Schmid et al., 1977). GSS
480 deformation involves a component of independent grain boundary sliding that is accommodated
481 by grain boundary diffusion ($n = 1$; Coble (1963)) or grain boundary dislocations ($n = 2$, Gifkins
482 (1976)).

483 In this study, the $n = 1.7$ and 2.0 determined for low dolomite experiments (Dm25 and
484 Dm35) suggest a component of GSS rheology. The low dolomite composites attain mechanical
485 steady state immediately following yield shear stress, which suggests the development of a stable
486 microstructure. Microstructurally, the calcite matrices comprise small, equidimensional,
487 polygonal grains that are strain free at the optical microscope and EBSD scale: a microstructure
488 typically associated with GSS creep (Rutter, 1974; Schmid, 1976; Schmid et al., 1977; Walker et
489 al., 1990). In addition, we do not observe any subgrains and there is no evidence for dynamic
490 recrystallization. Furthermore, grain size distributions of the starting and deformed materials
491 show limited change in calcite grain size; the grain size data calculated from EBSD processes
492 record neither significant grain growth nor grain size reduction in the deformed samples.

493 Preliminary TEM observations of the calcite aggregates show that dislocations are
494 abundant while subgrains are absent (Figure 11). The dislocation density and the absence of

495 subgrains in tandem with polygonal grains meeting at triple junctions are consistent with shear
496 strain accommodated by independent grain boundary displacements (Langdon, 2006).
497 Reconciliation of the experimental and textural data is accomplished by considering mixed-mode
498 deformation of the calcite aggregates including: independent grain boundary sliding,
499 intracrystalline dislocation glide, and diffusion creep (Casey et al., 1997). This behaviour is
500 characterized by near Newtonian flow ($n = 1$; typically $1 < n < 3$ for constitutive equations of the
501 form $\dot{\gamma} \propto \tau^n$) and is observed for temperatures > 0.5 the material's homologous temperature
502 (Langdon, 2006). We expect grains to be equiaxed, polygonal, strain free, and generally less than
503 10 microns in diameter. As a result of irregularities at grain boundaries and, especially, at the
504 junctions where more than two grains meet, independent grain boundary sliding is accomplished
505 by Rachinger sliding resulting in strain free, equiaxed grains. Grain boundary sliding also
506 encourages chemical exchange between phases, such as the transfer of Mg^{2+} between phases
507 observed in our experimental run-products, since neighbouring grains are constantly moving past
508 one another (Herwegh et al., 2003).

509 Critically, small quantities of Mg^{2+} in calcite limit grain growth, thereby keeping grain
510 size sensitive diffusion creep and grain boundary sliding operative during deformation (Herwegh
511 et al. (2003), even under high homologous conditions. Herwegh et al. (2003) found that calcite
512 grain size is inversely proportional to Mg-content, resulting in an extrinsic control on strength as
513 calcite grain growth is inhibited. In our experiments, Mg^{2+} migration from dolomite to calcite
514 confirms that diffusion creep processes occurred during deformation. Diffusion processes likely
515 contributed to maintaining the small calcite grain size throughout the experiments (Davis et al.,
516 2008; Delle Piane et al., 2009a; Delle Piane et al., 2008; Holyoke et al., 2013). Rybacki et al.
517 (2003) suggest that in the quartz-calcite system, Si incorporated into the dislocation cores of
518 calcite is responsible for the increase in flow strength of calcite. It is unknown if a similar
519 driving force exists in the calcite-dolomite system, though this cannot be discounted due to the
520 evidence for Mg^{2+} migration during deformation.

521 CPO development in the grain size sensitive field has been observed in dolomite (Delle
522 Piane et al., 2009a), calcite (Rutter et al., 1994a), olivine (Hansen et al., 2011; Sundberg and
523 Cooper, 2008), orthopyroxene (Sundberg and Cooper, 2008), forsterite (Miyazaki et al., 2013),
524 and ice (Goldsby and Kohlstedt, 2001). A CPO may occur in response to dislocation creep
525 accommodating relative grain boundary displacements (Ashby and Verrall, 1973; Langdon,
526 2006). However, Miyazaki et al. (2013) show that grain boundary orientation is often
527 crystallographically controlled with grain boundary sliding (GBS) frequently occurring on

528 specific planes. CPO development can, therefore, be a by-product of grain rotation by GBS
529 (Miyazaki et al., 2013). Critically, interface-controlled diffusion creep can lead to CPO
530 development despite little dislocation mobility; grain boundary sliding may be favoured in
531 systems where grain boundary anisotropy is significant thus precluding dislocation creep as the
532 dominant deformation mechanism (Sundberg and Cooper, 2008). Our J-indices are similar to
533 those calculated for Solnhofen limestone (Barnhoorn et al., 2005a) and fine-grained calcite-
534 dolomite composites (Delle Piane et al., 2009a) deformed to high shear strains; they are
535 significantly lower than those reported in synthetic, fine-grained calcite aggregates deformed to
536 high shear strains (Barnhoorn et al., 2005a). This likely results from the presence of a second
537 phase in our samples that curtails grain growth in the material, keeping the grain size small
538 (Barnhoorn et al., 2005a; Herwegh and Kunze, 2002; Olgaard, 1990) and hindering pervasive
539 dislocation mobility. Indeed, even nano-scale second phases are sufficient to pin grain
540 boundaries (Herwegh and Kunze, 2002); the fine-grained dolomite and minor accessory phases
541 in our samples are likely sufficient to pin grain boundaries, hampering grain growth and keeping
542 grain boundary sliding a dominant mechanism. The strength of the CPO for the calcite
543 aggregates and the lack of subgrains are consistent with grain boundary sliding assisted by
544 limited dislocation glide/creep (Rutter et al., 1994b; Schmid et al., 1987). Increased Mg^{2+}
545 mobility from dolomite to calcite (see Figure 14 and Supplementary Material) suggests that
546 diffusion processes are also active during deformation of our samples.

547 The microstructure and texture of calcite aggregates in all run products in this study
548 supports grain boundary sliding accommodated by diffusion creep and possible dislocation
549 glide/creep (Ashby and Verrall, 1973; Casey et al., 1997; Langdon, 2006; Mukherjee, 1975;
550 Schmid et al., 1977). Grain boundary diffusion results in the subtle elongation of calcite grains
551 and the solid-state diffusion processes that accommodate Mg^{2+} movement from dolomite into
552 calcite (Delle Piane et al., 2009a; Langdon, 2006). This is consistent with the more pronounced
553 grain elongation and Mg^{2+} movement observed in Dm75. Similar microstructures and textures
554 have been published on both 100%, fine-grained calcite (Casey et al., 1997; Schmid et al., 1977)
555 and fine-grained dolomite-calcite composites (Delle Piane et al., 2009a) and the same
556 deformation mechanisms have been proposed.

557 The most dolomite-rich experiment (P1538; Dm75) shows a mixed response to
558 deformation: fracture in dolomite and plastic flow of calcite. Mechanically, the Dm75 composite
559 is the strongest and the most complex: the material sustained a stress drop followed by the
560 attainment of stable flow after a shear strain of ~ 1 , followed by an episode of strain hardening

561 and strain softening (Figure 7A). The rheological behaviour of Dm75 is better described by
562 power law creep of calcite with Mohr Coulomb behavior in dolomite. The stress drop in Dm75
563 may have been a result of fracture of dolomite and reconfiguration of the material to attain an
564 interconnected network of calcite, thereby attaining stable flow.

565 *7.3 Deformation of Two-Phase Aggregates*

566 In our study, calcite is the weak phase. The addition of a second phase to a calcite matrix
567 can both strengthen (Austin et al., 2014; Barnhoorn et al., 2005b; Delle Piane et al., 2009a; Delle
568 Piane et al., 2009b; Rybacki et al., 2003) and weaken (Austin et al., 2014; Delle Piane et al.,
569 2009a) the composite aggregate. In fine-grained calcite aggregates that accommodate shear
570 strain primarily by grain boundary sliding, the addition of fine-grained dolomite strengthens the
571 aggregates at 700°C, but significantly weakens them at 800°C (Delle Piane et al., 2009a). This
572 strength inversion results from a loss of competence in fine-grained dolomite at high
573 temperatures and both dolomite and calcite deform by grain sensitive flow (Delle Piane et al.,
574 2009a). Our samples show significant strengthening with increasing dolomite content. This is, in
575 large part, due to the significant size of the dolomite grains, which act as rigid bodies and restrict
576 calcite flow in our samples.

577 Initially homogeneous, fine-grained, two-phase aggregates (e.g. anhydrite-calcite,
578 forsterite-pyroxene, and forsterite-diopside) develop compositional layering at high strain
579 (Barnhoorn et al., 2005a; Hiraga et al., 2013; Miyazaki et al., 2013). In fine-grained forsterite-
580 pyroxene aggregates, grain boundary sliding was shown to encourage ‘demixing’ of the mineral
581 phases through grain switching events, giving rise to compositional layering (Hiraga et al.,
582 2013). In our samples, the low-dolomite content (Dm 25 and Dm35) aggregates show
583 compositional layering at high strains. We attribute this layering to the deformation of the
584 spherical calcite aggregates present in the starting material and the segregation of coarse-grained
585 dolomite. We do not observe convincing ‘demixing’ of phases within our aggregates, probably
586 due to the large grain size of dolomite, which precludes the dolomite from participating in grain
587 boundary sliding. The 75% dolomite content sample has a crude compositional foliation
588 (because of dolomite grain size differentiation) defined by predominantly calcite and finer-
589 grained dolomite grains, alternating with coarse-grained dolomite. Because of their bimodal
590 grain size distribution (fine-grained calcite and coarse-grained dolomite) the behaviour of our
591 samples is not consistent with the ‘demixing’ of phases via grain switching events but instead by
592 mechanical sorting based on grain size.

593 7.4 Calcite Aggregates: Analogues for Veins in Nature?

594 EBSD analysis of the compositionally homogeneous calcite bands present in P1527 and
595 P1524 (Figures 8A, 8B, and 12) show stronger CPOs in these regions than in the surrounding
596 calcite-dolomite matrix. This suggests that these layers record more applied shear strain (Rutter
597 et al., 1994b). Additionally, the presence of deflected foliations suggests strain partitioning and
598 localization (refer to Figure 8B): areas rich in dolomite accommodated less displacement (i.e. are
599 less sheared) than monomineralic calcite layers. Strain partitioning may occur because
600 compositionally homogeneous regions are more easily deformed as grain boundary pinning is
601 not encouraged (Olgaard, 1990). This results in the maintenance of the initial compositional
602 zoning of the samples.

603 These calcite regions provide an interesting analog for calcite veins in nature that are
604 observed to absorb more strain than the surrounding host rock (Kennedy and White, 2001). Low
605 chemical potential gradients between single phase grains inhibit diffusion processes, leading to
606 the activation of dislocation glide and, ultimately, back-stressing from the pileup of dislocations
607 at grain boundaries, resulting in a population of strain free grains with similar CPO (Kennedy
608 and White, 2001; Molli et al., 2011). This effect is more pronounced in pure calcite regions of
609 Dm25 and Dm35 because the chemical potential gradients between grains are such that diffusion
610 processes are curtailed (Kennedy and White, 2001).

611 8. Conclusions

612 The styles and mechanisms of deformation associated with many variably dolomitized
613 limestone shear systems are strongly controlled by strain partitioning between dolomite and
614 calcite. The contrasting deformation behaviour of dolomite and calcite aggregates in our
615 experiments is fundamentally related to grain size. Fine-grained calcite (and possibly dolomite)
616 deform by grain boundary sliding assisted by diffusion creep and possible limited dislocation
617 glide. In low dolomite composites, dolomite grains act to increase the strength of shear zones
618 relative to 100% calcite, presumably because the fine-grained calcite must flow around rigid
619 dolomite grains.

620 In high dolomite content samples, two deformation mechanisms likely occur
621 concomitantly (either in parallel or in series) during shear: brittle failure of dolomite and
622 superplastic flow of calcite. We infer that strain hardening occurs until dolomite grains fracture
623 permitting interconnected, fine-grained calcite to form crude layers such that grain boundary
624 sliding of fine-grained calcite accommodates displacement. This results in extreme localization

625 of shear strain into thin, discontinuous calcite layers. These calcite layers are periodically
626 obstructed by clusters of coarse-grained dolomite leading to further locking of the system. With
627 increased dolomite content, a stress exponent greater than 3 indicates that 75% dolomite can still
628 be described by power-law models, however, based on the microstructure, brittle deformation
629 (Mohr –Coulomb) should be considered to act intermittently during shear strain.

630 These observations are critical to the interpretation of fault systems where dolomite may
631 periodically inhibit flow in calcite networks, thereby locking the fault system and resulting in the
632 build up of shear stresses. We speculate that the embrittlement of dolomite within these zones
633 may be necessary in the re-establishment of grain boundary sliding networks in calcite leading to
634 a continued ductile response of such systems.

635

636

637 Acknowledgements:

638 Our sincerest thanks are extended to J.K. Russell for his advice and support during the
639 experimental program and writing process. Special thanks to Rolf Bruijn and Richard Bakker for
640 their technical assistance and support during the deformation experiments at ETH-Zürich.
641 Chadwick Sinclair, Jacob Kabel, and Jacques Precigout are sincerely thanked for their assistance
642 and advice regarding EBSD analysis. Edith Czech and Jenny Lai are thanked for technical
643 support during SEM and microprobe work. This manuscript benefited greatly from the editorial
644 guardianship of Ian Alsop and enriching reviews from Auke Barnhoorn and an anonymous
645 reviewer. TEM analysis was carried out at the Microscopy and Microanalysis Facility at the
646 University of New Brunswick. Funding for Alexandra Kushnir was provided by the Alexander
647 Graham Bell Canada Scholarship from the National Sciences and Engineering Research Council
648 of Canada and Campus France. J.C. White and L.A. Kennedy were independently funded by
649 National Sciences and Engineering Research Council of Canada Discovery Grants.

650

651 **Figure Captions**

652

653 Figure 1. Grain size distributions (vol.%) of starting material powders. A. Grain size
654 distributions of pure calcite and pure dolomite powders. Modal grain sizes of the calcite and
655 dolomite powders are 9 μm and 120 μm , respectively. B. Grain size distributions of calcite-
656 dolomite powder mixtures used for fabricating the synthetic composites.

657

658 Figure 2. Scanning electron microscopy (SEM) and electron backscatter diffraction (EBSD)
659 analysis of Dm25 and Dm75 starting materials after synthesis. The a and b axes refer to the axes
660 on the stereographic projections. The cold pressing direction is parallel to the canister length,
661 into the page. A. Dm25; Equiaxed calcite grains, closely packed with straight grain boundaries
662 forming triple junctions. There is significant residual intergranular porosity at calcite grain
663 boundaries. B. Dm25; Lower hemisphere contoured stereoplots for the c slip system for calcite
664 (left) and dolomite (right). N is the number of grains used to produce the pole figures, J is the J-
665 texture index, and pfJ is the pole figure J-texture index, reflecting texture strength of the c-slip
666 system. C. Dm75; Equiaxed calcite grains, closely packed with straight grain boundaries forming
667 triple junctions. Residual porosity is concentrated at dolomite boundaries. D. Dm75. Lower
668 hemisphere contoured stereoplots for the c slip system for calcite (left) and dolomite (right). N is
669 the number of grains used to produce the pole figures, J is the J-texture index, and pfJ is the pole
670 figure J-texture index, reflecting texture strength of the c-slip system. Note the large variation in
671 dolomite grain size that is also common in naturally formed dolomitic limestones.

672

673 Figure 3. Backscatter electron images of a pure calcite spherical aggregate in Dm35 starting
674 material. A. The diameter of the imaged aggregate is $\sim 200 \mu\text{m}$. B. High aspect ratio dolomite
675 grains are oriented such that their long axes are tangential to the circumference of the aggregate.
676 The dashed white line identifies the boundary between pure calcite and calcite-dolomite.
677 Porosity within the aggregate is homogeneously distributed and occurs along calcite grain
678 boundaries, specifically at triple junctions.

679

680 Figure 4. Grain size distributions (area fraction) of calcite (A) and dolomite (B) from coherent,
681 hot isostatically pressed starting material and high strain experiments (Dm25, P1527; Dm75,
682 P1538) measured using SEM and EBSD techniques.

683

684 Figure 5. A. Schematic of the Paterson deformation apparatus with torsion actuator (modified
 685 from Paterson and Olgaard, (2000)). B. Schematic diagram of the two principal thin section cuts
 686 used in this study (Paterson and Olgaard, (2000)). The longitudinal axial cut captures
 687 intermediate strains along the centre axis of the segment. The longitudinal tangential segment
 688 captures the maximum strain plane of the sample. d and l are the diameter and length of the
 689 perfect cylindrical sample, respectively.

690

691 Figure 6. Log-log plot of shear strain rate vs. torque from the strain rate stepping experiments for
 692 A. Dm25 and Dm35 and, B. Dm75; the slope of the lines of best fit are the n -values (stress
 693 exponent, Eq. (4)) for the given compositions. Experimental conditions: $T=750^{\circ}\text{C}$; $P_{\text{eff}} = 262$
 694 MPa.

695

696 Figure 7. Mechanical data for A. high-strain-rate experiments and B. low-strain-rate
 697 experiments. See Table 2 for experimental conditions. High-strain-rate experiments: P1522
 698 (Dm25), P1524 (Dm35), P1525 (Dm75), P1527 (Dm25), P1528 (Dm51), P1537 (Dm51), and
 699 P1538 (Dm75). The heating history of experiment P1537 (Dm51) is not known for shear strains
 700 above 2, therefore, this data is omitted. Low strain experiments: P1523 (Dm51), P1533 (Dm75),
 701 and P1543 (Dm35). C. Shear stress as a function of dolomite content. Shear stress increases with
 702 dolomite content. Triangles denote yield stress; squares denote the shear stress at a shear strain
 703 equal to 1.5; circles denote peak shear stress. Shear stresses for 0%, 9%, 40%, and 100%
 704 dolomite contents are taken from Barnhoorn et al. (2005a), Delle Piane et al. (2009a), Davis et
 705 al. (2008), and Holyoke et al. (2013). Equivalent shear stresses for the reported differential
 706 stresses in Davis et al. (2008) and Holyoke et al. (2013) were calculated using Paterson and
 707 Olgaard (2000).

708

709 Figure 8. SEM images. Dolomite is the larger, dark grey phase. Calcite makes up the light grey
 710 matrix. Pyrite is white. High strain, deformed material: Dm25; P1527; $\gamma \sim 5$; 750°C ; $3 \times 10^{-4} \text{ s}^{-1}$.
 711 Longitudinal tangential plane (refer to Figure 5B). The shear zone boundary is horizontal in all
 712 images. A. Foliation is defined by elongate calcite aggregates (dashed ellipse). Shear strain is
 713 calculated by $\gamma = \cot \alpha' - \cot \alpha$. B. The foliation in the bulk calcite-dolomite matrix is deflected
 714 and converges with the higher strained pure-calcite band (oriented sub-parallel to the shear zone
 715 boundary). Dashed white lines delineate the bulk foliation within the sample. Dashed black line
 716 delineates the boundaries of the pure-calcite band. C. C-s mylonite texture. Foliation is defined

717 by surfaces of apparent localized strain (black rectangle), elongate pyrite grains, and rotated,
718 high aspect ratio dolomite grains (black arrows). Dolomite grains are organized along both s-
719 and c-foliations and are not obviously rounded. D. Localised c-surfaces appear as thin, dark,
720 discontinuous layers defined by ultrafine-grained material. A selection of c-surfaces are
721 highlighted by arrows. E. Closely packed, equiaxed to tabular calcite-grains. Grain boundaries
722 form triple junctions and are generally straight. Note significant isolated porosity. F.
723 Considerable isolated porosity located within 'pressure shadow'-like regions of dolomite grains.
724

725 Figure 9. SEM images. Dolomite is the larger, dark grey phase. Calcite makes up the light grey
726 matrix. Pyrite is white. High strain deformed material: Dm75. P1538; $\gamma \sim 5$; 750°C ; $3 \times 10^{-4} \text{ s}^{-1}$.
727 Longitudinal tangential plane (refer to Figure 5B); the shear zone boundary (SZB) is horizontal
728 in all images. A. Patchy foliation development in Dm75 where tabular dolomite is rotated to
729 define a shape fabric (centre of the image). The pyrite grain in the top left hand corner (white)
730 has been boudinaged and deformed around the more rigid dolomite grain. The white ellipse
731 highlights a dolomite grain that has fragmented by shear fracture during sinistral shear. B.
732 Closely packed, equiaxed to elongate calcite grains. Rounded, tabular dolomite grains are rotated
733 into foliation. C. Evidence of ductile deformation. The dashed black line defines the local
734 foliation developed within the calcite matrix. The foliation is deflected around large dolomite
735 grains. A highly sheared pyrite grain is identified by the white arrow. D. Antithetic shear fracture
736 of a large dolomite grain.

737
738 Figure 10. EBSD analysis of high strain experiments, Dm25 (P1527) and Dm75 (P1538). The
739 shear zone boundary (SZB) is horizontal in all images and pole figures. N is the number of
740 grains used to produce the pole figures, J is the J-texture index, and pfJ is the pole figure J-
741 texture index, reflecting texture strength of the individual slip systems. A. Dm25; low
742 magnification BSE image. B. Dm25. Calcite: EBSD map (top); lower hemisphere contoured
743 stereoplots (bottom) for the c and a slip systems. C. Dm25. Dolomite: EBSD map (top); lower
744 hemisphere contoured stereoplots (bottom) for the c and a slip systems. Blackened portions of
745 the EBSD maps are components of different phases, not indexed. See text for details. D. Dm75;
746 low magnification BSE image. E. Dm75. Calcite: EBSD map (top); lower hemisphere contoured
747 stereoplots (bottom) for the c and a slip systems. F. Dm75. Dolomite: EBSD map (top); lower
748 hemisphere contoured stereoplots (bottom) for the c and a slip systems. Blackened portions of
749 the EBSD maps are components of different phases, not indexed. See text for details.

750

751 Figure 11. Transmission electron microscopy (TEM BF). A. Glide dislocations within calcite
752 grain. B. Equant grain texture in deformed calcite consistent with grain boundary sliding
753 (superplasticity). Despite the absence of grain shape change (elongation), there are high
754 dislocation densities within individual grains, suggesting creep accommodated grain boundary
755 sliding.

756

757 Figure 12. Crystallographic preferred orientation development near calcite aggregates. The shear
758 zone boundary (SZB) is horizontal in all BSE images and EBSD maps. N is the number of grains
759 used to produce the pole figures, J is the J-texture index, and pfJ is the pole figure J-texture
760 index, reflecting texture strength of the individual slip systems. All pole figures are lower
761 hemisphere projections. A. BSE image of Dm25 sample deformed to $\gamma \sim 5.5$ (see Table 2; P1527).
762 A calcite sphere that has been sheared into an ellipsoid is delineated by the red lines. B. EBSD
763 map and stereonet projection of the c and a slip systems in calcite across the deformed calcite
764 band. C. EBSD map and stereonet projection of calcite in a region removed from the calcite band.
765 D. EBSD map and stereonet projections of a region adjacent to the calcite band, but including
766 dolomite grains. E. EBSD map and stereonet projection of a region within the calcite band.

767

768 Figure 13. Evolution of crystallographic preferred orientation (CPO) of the c-axis slip system in
769 calcite with strain. Stress-strain curves represent the stress-strain conditions at the sample edge.
770 Stereonets are lower hemisphere projections; shear zone boundary (SZB) is horizontal. For a
771 given composition, each stereonet is produced by analysing a different longitudinal axial section
772 from the same deformed core (see Figure 5B), thus representing the state of the material at
773 different shear strains. N is the number of grains used to produce the pole figures, J is the J-
774 texture index, and pfJ is the pole figure J-texture index, reflecting texture strength of the c-axis
775 slip system. Red dots indicate the approximate points on the stress-strain curve that correspond
776 to the longitudinal axial cuts made. CPO becomes more defined with increasing shear strain (i.e.
777 the c-axis girdle becomes more narrow with increasing strain and the J- and pfJ-indices generally
778 increase, with the exception of C). A. Dm25 (P1527). B. Dm35 (P1524). C. Dm75 (P1538).

779

780 Figure 14 Energy-dispersive X-ray spectroscopy (EDS) maps of magnesium concentration for
781 experiment P1527. Experimental conditions: $P_{\text{eff}}=262$ MPa, $T=750^\circ\text{C}$, and strain rate $3 \times 10^{-4} \text{ s}^{-1}$.
782 The shear zone boundary (SZB) is horizontal in all images. A. EDS map of a longitudinal axial

783 section of the sample corresponding to $\gamma \sim 0$ (see Figure 5B). B. EDS map of a longitudinal axial
784 section of the sample corresponding to $\gamma \sim 2.25$. C. EDS map of the longitudinal tangential section
785 of the sample, corresponding to $\gamma \sim 5.5$. White grains are dolomite. The calcite matrix contains
786 very little magnesium and, therefore, is black. For $\gamma \sim 0$, there is no magnesium observed within
787 the matrix. With increasing strain, Mg^{2+} concentrations increase in the matrix; note the increase
788 in white streaking between dolomite grains in B and C. This only occurs in regions of the sample
789 with locally significant fine-grained dolomite content. With increasing shear strain, Mg^{2+}
790 becomes more concentrated along the developing foliation of the sample.

791

792 Figure 15 A. Comparison of the study data with the reported deformation mechanism map of
793 Solnhofen limestone (taken from Schmid et al., 1977). Log-log plot of the differential stress vs.
794 strain rate for compression deformation experiments on Solnhofen limestone. Regime 1:
795 Exponential relationship between strain rate and stress; Regime 2: Power-law creep; Regime 3:
796 Superplasticity. Regimes 1 and 2 are characterized in the microstructure by dislocation glide
797 and/or dislocation creep. Regime 3 is characterized in the microstructure by grain boundary
798 sliding. Triangles indicate data from this study. With increasing differential stress, these triangles
799 represent the peak strengths of Dm25, Dm35, Dm51, and Dm75. The square and circle indicate
800 the peak stress for Solnhofen limestone deformed by torsion to high strains at 700°C and 800°C,
801 respectively (Schmid et al., 1987). B. Comparison of study data with reported deformation
802 behaviour of Madoc dolomite (Davis et al., 2008; Holyoke et al., 2013). The deformation
803 mechanism map is taken from Holyoke et al. (2013) and is contoured for dolomite grain size.
804 The contours denote the transition between dislocation creep and diffusion creep. Experiment
805 P1538 (Dm75, taken to high strain) is plotted as a triangle and lies in the diffusion creep field for
806 dolomite grain sizes $< 10 \mu m$ and the dislocation creep field for dolomite grain sizes $> 100 \mu m$.
807 The square and circle represent the differential stress of Madoc dolomite (grain size = $240 \mu m$) at
808 700°C (Davis et al., 2008) and 900°C (Holyoke et al., 2013), respectively.

809

810 **References**

- 811 Ashby, M.F., Verrall, R.A., 1973. Diffusion-accommodated flow and superplasticity. *Acta*
812 *Metall.* 21, 149-163.
- 813 Austin, N.J., 2003. An experimental investigation of textural controls on the brittle deformation
814 of dolomite, *Earth and Ocean Sciences*. University of British Columbia, Vancouver.
- 815 Austin, N.J., Evans, B., Rybacki, E., Dresen, G., 2014. Strength evolution and the development
816 of crystallographic preferred orientation during deformation of two-phase marbles.
817 *Tectonophysics* 631, 14-28.
- 818 Austin, N.J., Kennedy, L.A., 2005. Textural controls on the brittle deformation of dolomite:
819 variations in peak strength. *Geological Society Special Publication*, 37-49.
- 820 Austin, N.J., Kennedy, L.A., Logan, J.M., Rodway, R., 2005. Textural controls on the brittle
821 deformation of dolomite: The transition from brittle faulting to cataclastic flow. *Geological*
822 *Society Special Publication*, 51-66.
- 823 Bachmann F., H., R., Schaeben, H., 2010. Texture Analysis with MTEX - Free and Open Source
824 Software Toolbox. *Solid State Phenomena* 160, 63-68.
- 825 Barnhoorn, A., 2003. Rheological and microstructural evolution of carbonate rocks during large
826 strain torsion experiments. Swiss Federal Institute of Technology Zurich, ETH Zurich.
- 827 Barnhoorn, A., Bystricky, M., Burlini, L., Kunze, K., 2005a. Post-deformational annealing of
828 calcite rocks. *Tectonophysics* 403, 176-191.
- 829 Barnhoorn, A., Bystricky, M., Kunze, K., Burlini, L., Burg, J.P., 2005b. Strain localisation in
830 biminerale rocks: Experimental deformation of synthetic calcite-anhydrite aggregates. *Earth and*
831 *Planetary Science Letters* 240, 748-763.
- 832 Bestmann, M., Kunze, K., Matthews, A., 2000. Evolution of a calcite marble shear zone complex
833 on Thassos Island, Greece: microstructural and textural fabrics and their kinematic significance.
834 *Journal of Structural Geology* 22, 1789-1807.
- 835 Casey, M., Kunze, K., Olgaard, D.L., 1997. Texture of Solnhofen limestone deformed to high
836 strains in torsion. *Journal of Structural Geology* 20, 255-267.
- 837 Coble, R.L., 1963. A model for boundary diffusion controlled creep in polycrystalline materials.
838 *Journal of Applied Physics*.
- 839 Davis, N.E., Kronenberg, A.K., Newman, J., 2008. Plasticity and diffusion creep of dolomite.
840 *Tectonophysics*, 127-146.
- 841 Delle Piane, C., Burlini, L., Kunze, K., 2009a. The influence of dolomite on the plastic flow of
842 calcite: Rheological, microstructural and chemical evolution during large strain torsion
843 experiments. *Tectonophysics*, 145-166.
- 844 Delle Piane, C., Burlini, L., Kunze, K., Brack, P., Burg, J.P., 2008. Rheology of dolomite: Large
845 strain torsion experiments and natural examples. *Journal of Structural Geology* 30, 767-776.
- 846 Delle Piane, C., Wilson, C.J.L., Burlini, L., 2009b. Dilatant plasticity in high-strain experiments
847 on calcite-muscovite aggregates. *Journal of Structural Geology*, 1084-1099.
- 848 Erikson, S.G., 1994. Deformation of shale and dolomite in the Lewis Thrust-fault zone,
849 Northwest Montana, USA. *Canadian Journal Earth Sciences* 31, 1440-1448.
- 850 Gifkins, R.C., 1976. Grain-boundary sliding and its accommodation during creep and
851 superplasticity. *Metallurgical Transactions A-Physical Metallurgy and Material Science* 7, 1225-
852 1232.
- 853 Goldsby, D.L., Kohlstedt, D.L., 2001. Superplastic deformation of ice: Experimental
854 observations. *Journal of Geophysical Research*, 11017-11030.
- 855 Goldsmith, J.R., 1959. Some aspects of the geochemistry of carbonates.
- 856 Griggs, D.T., Turner, F.J., Borg, I., Sosoka, J., 1951. Deformation of Yule marble, part iV.
857 Effects at 150C. *GSA Bulletin* 62, 1385-1486.

- 858 Griggs, D.T., Turner, F.J., Borg, I., Sosoka, J., 1953. Deformation of Yule marble, part V.
859 Effects at 300C. GSA Bulletin 64.
- 860 Handin, J., Fairburn, H.W., 1955. Experimental deformation of Hasmark dolomite. GSA Bulletin
861 66, 1257-1274.
- 862 Hansen, L.N., Zimmerman, M.E., Kohlstedt, D.L., 2011. Grain boundary sliding in San Carlos
863 olivine: Flow law parameters and crystallographic-preferred orientation. Journal of Geophysical
864 Research 116.
- 865 Herwegh, M., De Bresser, J.H.P., ter Heege, J.H., 2005. Combining natural microstructures with
866 composite flow laws: an improved approach for the extrapolation of lab data to nature. Journal of
867 Structural Geology, 503-521.
- 868 Herwegh, M., Kunze, K., 2002. The influence of nano-scale second-phase particles on
869 deformation of fine grained calcite mylonites. Journal of Structural Geology 24, 1463-1478.
- 870 Herwegh, M., Xiao, X., Evans, B., 2003. The effect of dissolved magnesium on diffusion creep
871 in calcite. Earth and Planetary Science Letters 212, 457-470.
- 872 Higgs, D.V., Handin, J., 1959. Experimental deformation of dolomite single crystals. Bulletin of
873 the Geological Society of America 70.
- 874 Hiraga, T., Miyazaki, T., Yoshida, H., Zimmerman, M.E., 2013. Comparison of microstructures
875 in superplastically deformed synthetic materials and natural mylonites: Mineral aggregation via
876 grain boundary sliding. Geology 41, 959-962.
- 877 Holyoke, C.W., Kronenberg, A.K., Newman, J., 2013. Dislocation creep of polycrystalline
878 dolomite. Tectonophysics 590, 72-82.
- 879 Kennedy, L.A., Logan, J.M., 1997. The role of veining and dissolution in the evolution of fine-
880 grained mylonites: the McConnell thrust, Alberta. Journal of Structural Geology 19, 785-797.
- 881 Kennedy, L.A., White, J.C., 2001. Low-temperature recrystallization in calcite: Mechanisms and
882 consequences. Geology 29, 1027-1030.
- 883 Langdon, T.G., 2006. Grain boundary sliding revisited: Developments in sliding over four
884 decades. Journal of Material Sciences, 597-609.
- 885 Miyazaki, T., Sueyoshi, K., Hiraga, T., 2013. Olivine crystals align during diffusion creep of
886 Earth's upper mantle. Nature 502, 321-326.
- 887 Molli, G., White, J.C., Kennedy, L.A., Taini, V., 2011. Low-temperature deformation of
888 limestone, Isola Palmaria, northern Apennine, Italy - The role of primary textures, precursory
889 veins and intracrystalline deformation in localization. Journal of Structural Geology, 225-270.
- 890 Mukherjee, A.K., 1975. High-temperature creep. Academic Press, New York.
- 891 Olgaard, D.L., 1990. The role of second phase in localizing deformation, in: Knipe, R.J., Rutter,
892 E.H. (Eds.), Deformation Mechanisms, Rheology and Tectonics. Geological Society Special
893 Publication, pp. 175-181.
- 894 Paterson, M.S., Olgaard, D.L., 2000. Rock deformation tests to large shear strains in torsion.
895 Journal of Structural Geology 22, 1341-1358.
- 896 Pera, E., Mainprice, D., Burlini, L., 2003. Anisotropic seismic properties of the upper mantle
897 beneath the Torre Alfina area (Northern Apennines, Central Italy). Tectonophysics, 11-30.
- 898 Pouchou, J.L., Pichoir, F., 1985. PAP $\phi(\rho Z)$ procedure for improved quantitative microanalysis.
899 Microbeam Analysis, 104-106.
- 900 Raudsepp, M., Pani, E., Dipple, G.M., 1999. Measuring mineral abundance in skarn. I. The
901 Rietveld method using X-ray powder diffraction data. Canadian Mineralogist 37, 1-15.
- 902 Rutter, E., 1974. The influence of temperature, strain rate and interstitial water in experimental
903 deformation of calcite rocks. Tectonophysics 22, 311-334.
- 904 Rutter, E., Casey, M., Burlini, L., 1994a. Preferred crystallographic orientation development
905 during the plastic and superplastic flow of calcite rocks. Journal of Structural Geology 16, 1431-
906 1446.

- 907 Rutter, E.H., Casey, M., Burlini, L., , 1994b. Preferred crystallographic orientation development
908 during the plastic and superplastic flow of calcite rocks. *Journal of Structural Geology* 16, 1431-
909 1446.
- 910 Rybacki, E., Paterson, M.S., Wirth, R., Dresen, G., 2003. Rheology of calcite-quartz aggregates
911 deformed to large strain in torsion. *Journal of Geophysical Research* 108, 2089.
- 912 Schmid, S.M., 1976. Rheological evidence for changes in the deformation mechanism of
913 Solnhofen limestone towards low stress. *Tectonophysics* 31, T21-T28.
- 914 Schmid, S.M., Boland, J.N., Paterson, M.S., 1977. Superplastic flow in Finegrained limestone.
915 *Tectonophysics*, 257-291.
- 916 Schmid, S.M., Panozzo, R., Bauer, S., 1987. Simple shear experiments on calcite rocks: rheology
917 and microfabric. *Journal of Structural Geology* 9, 747-778.
- 918 Sundberg, M., Cooper, R.F., 2008. Crystallographic preferred orientation produced by diffusional
919 creep of harzburgite: Effects of chemical interactions among phases during plastic flow. *Journal*
920 *of Geophysical Research* 113.
- 921 Viola, G., Mancktelow, N.S., Miller, J.A., 2006. Cyclic frictional-viscous slip oscillations along
922 the base of an advancing nappe complex: Insights into brittle-ductile nappe emplacement
923 mechanisms from the Naukluft Nappe Complex, central Namibia. *Tectonics* 25.
- 924 Walker, A.N., Rutter, E.H., Brodie, K.H., 1990. Experimental study of grain-size sensitive flow
925 of synthetic, hot pressed calcite rocks, in: Knipe, R.J., Rutter, E.H. (Eds.), *Deformation*
926 *Mechanisms, Rheology and Tectonics*. *Geologic Society Special Publications*, pp. 259-284.
- 927 Weertman, J., 1957. Steady-state creep through dislocation climb. *Journal of Applied Physics*,
928 362-364.
- 929 Woodward, N.B., Wojtal, S., Paul, J.B., Zadins, Z.Z., 1988. Partitioning of deformation within
930 several external thrust zones of the Appalachian orogen. *J. Geol.* 96, 351-361.
- 931

Table 1. Properties of HIP samples: dolomite content (Dm), connected porosity (ϕ), density (ρ).

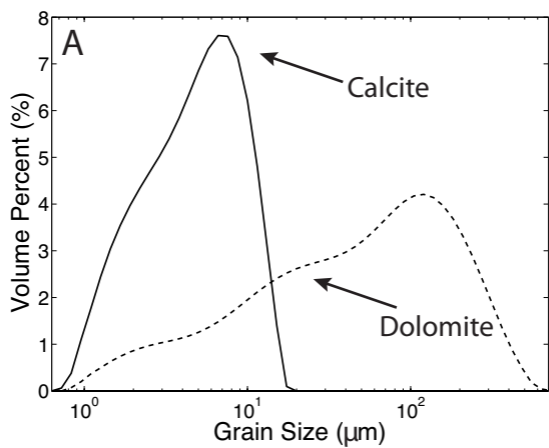
Dm (%)	ϕ (%)	ρ (kg m ⁻³)
25	3.3±0.2	2.76
35	3.3±0.2	2.77
51	2.7±0.3	2.80
75	5.2±0.3	2.85

Table 2 List of deformation experiments performed and results.

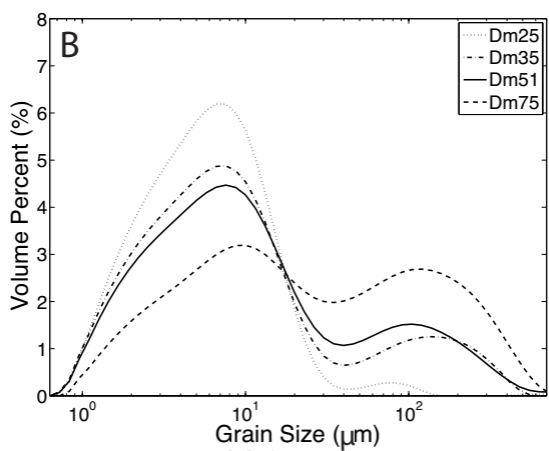
Experiment	Dm (%)	T (°C)	P _C (MPa)	P _e (MPa)	$\dot{\gamma}$ (s ⁻¹)	$\dot{\gamma}_{cont}$	τ_{yield} (MPa)	τ_{peak} (MPa)	$\tau_{\gamma=1.5}$ (MPa)	<i>n</i>
Constant Strain Rate Experiments										
P1522	25	750	300	262	3x10 ⁻⁴	4.4	33	79	33	
P1523	51	750	300	262	1x10 ⁻⁴	1.9	17	77	-	
P1524	35	750	300	262	3x10 ⁻⁴	5	33	79	33	
P1525	75	750	300	262	3x10 ⁻⁴	0.16	36	117	-	
P1527	25	750	300	262	3x10 ⁻⁴	5.5	27	82	27	
P1528	51	750	300	262	3x10 ⁻⁴	0.21	28	79	-	
P1533	75	750	300	262	1x10 ⁻⁴	0.17	44	92	-	
P1537	51	750	300	262	3x10 ⁻⁴	1.7	35	135	35	
P1538	75	750	300	262	3x10 ⁻⁴	5.5	57	167	37	
P1543	35	750	300	262	1x10 ⁻⁴	0.1	12	63	-	
Strain Rate Stepping Experiment										
P1529	35	750	300	262	stepping	n.d.	-	-	-	2.0±0.43
P1711	25	750	300	262	stepping	n.d.	-	-	-	1.7±0.23

P1713	75	750	300	262	stepping	n.d.	3.6±0.12
-------	----	-----	-----	-----	----------	------	----------

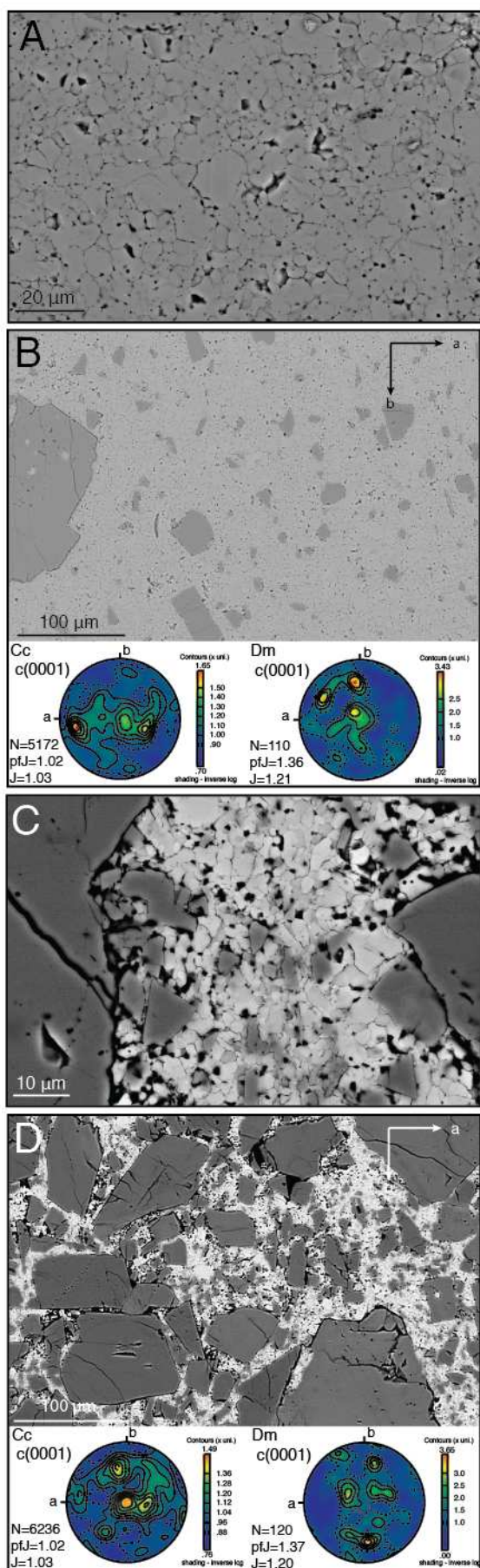
n.d. not determined, Dm – dolomite content (%), T – temperature (°C), P_c – confining pressure (MPa), P_e – confining pressure (MPa), $\dot{\gamma}$ – shear strain rate (s⁻¹), τ_{max} – maximum shear stress, n – stress exponent, τ_{yield} – yield strength (MPa), τ_{peak} – peak strength (MPa), $\tau_{\gamma=1.5}$ – strength at a shear strain of 1.5 (MPa).



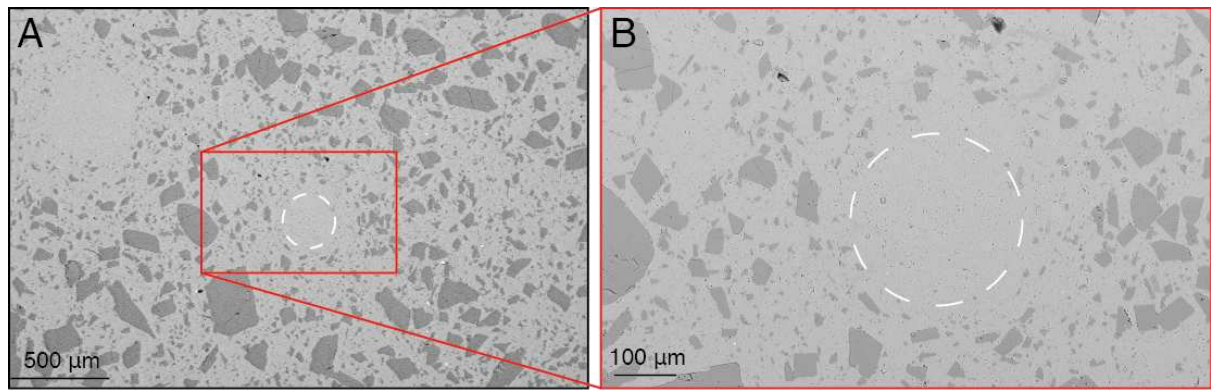
ACCEPTED MANUSCRIPT



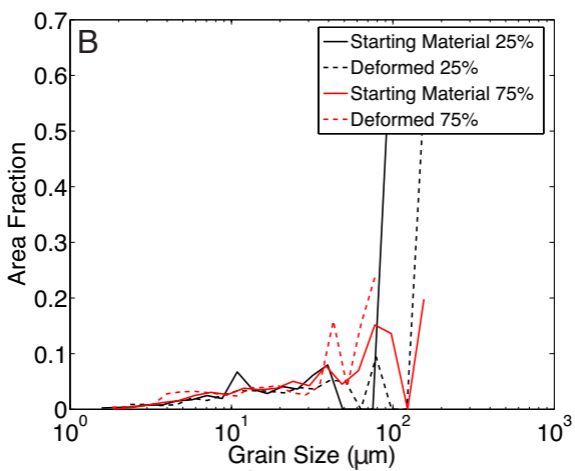
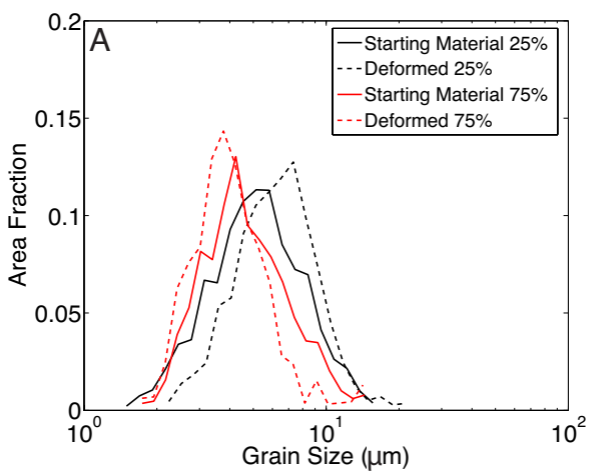
ACCEPTED



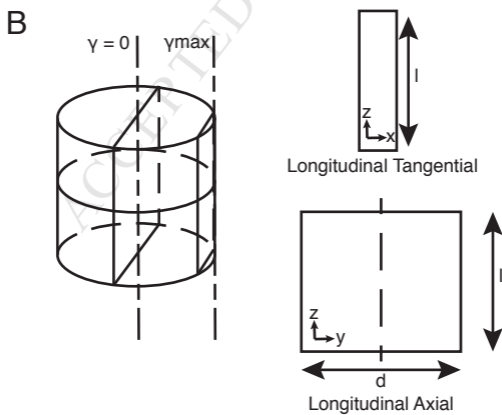
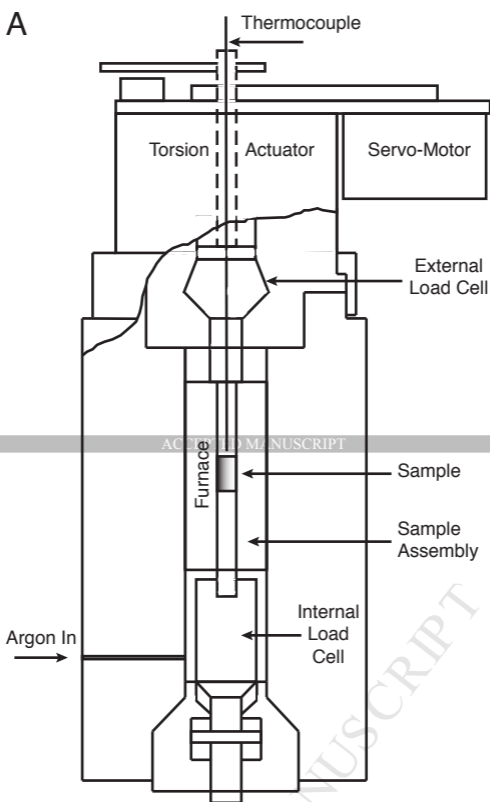
MANUSCRIPT

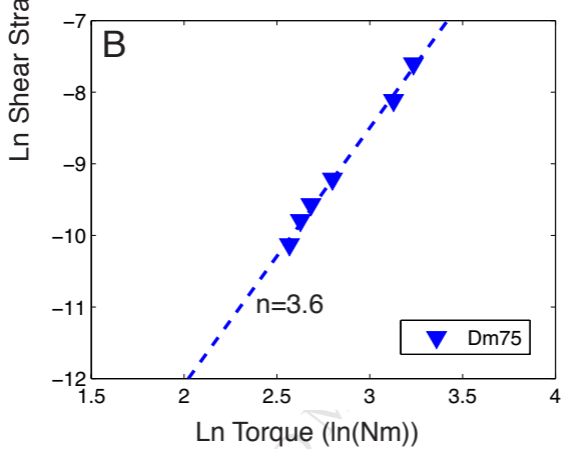
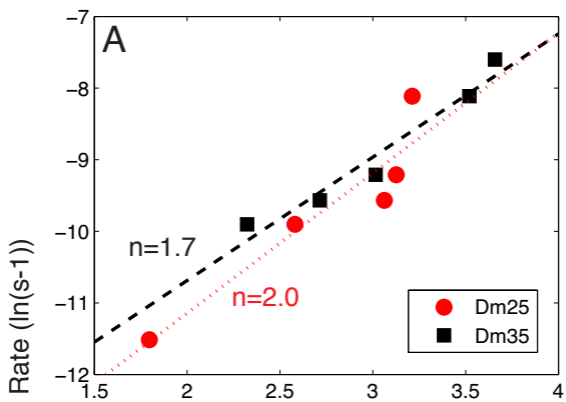


ACCEPTED MANUSCRIPT

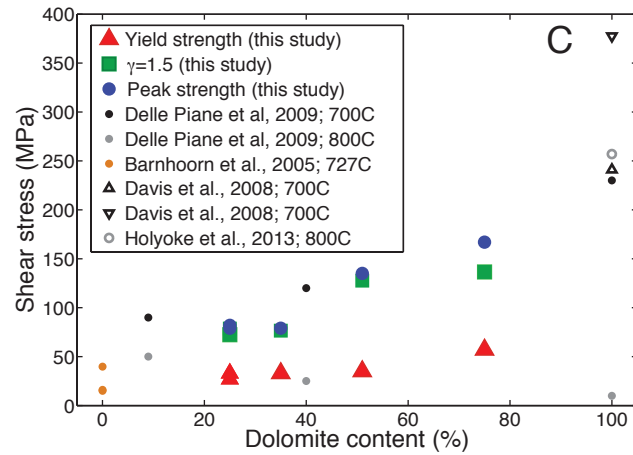
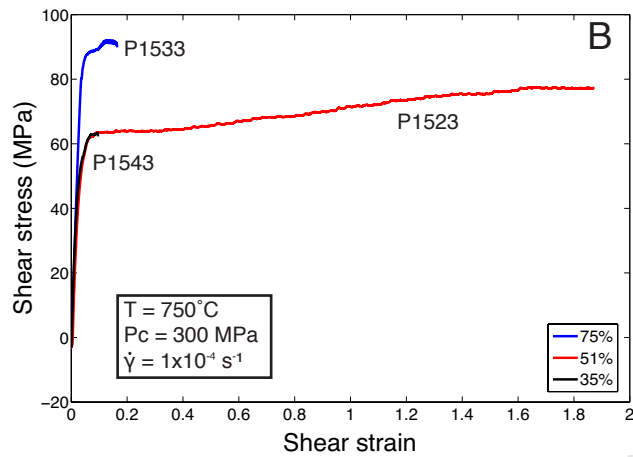
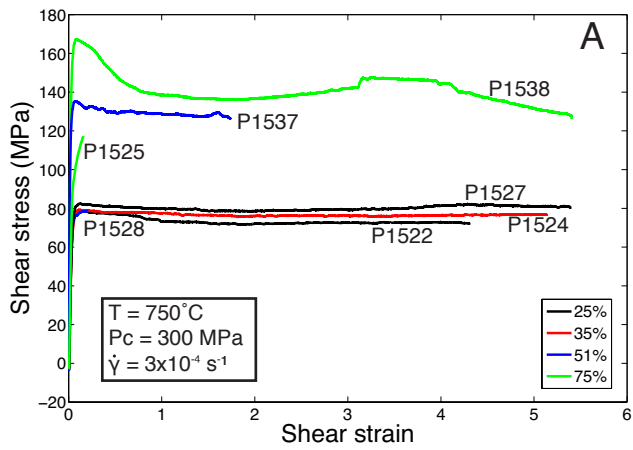


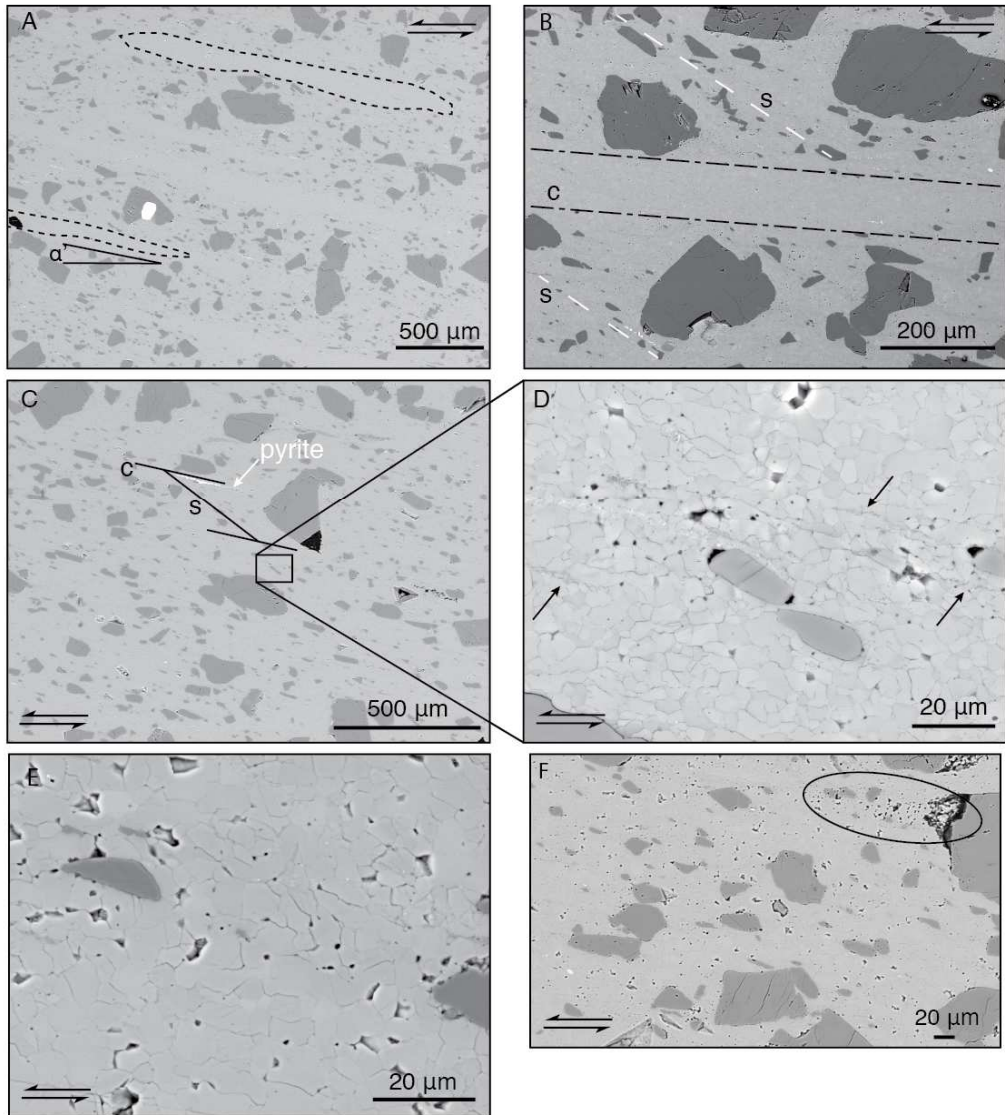
ACCEPTED

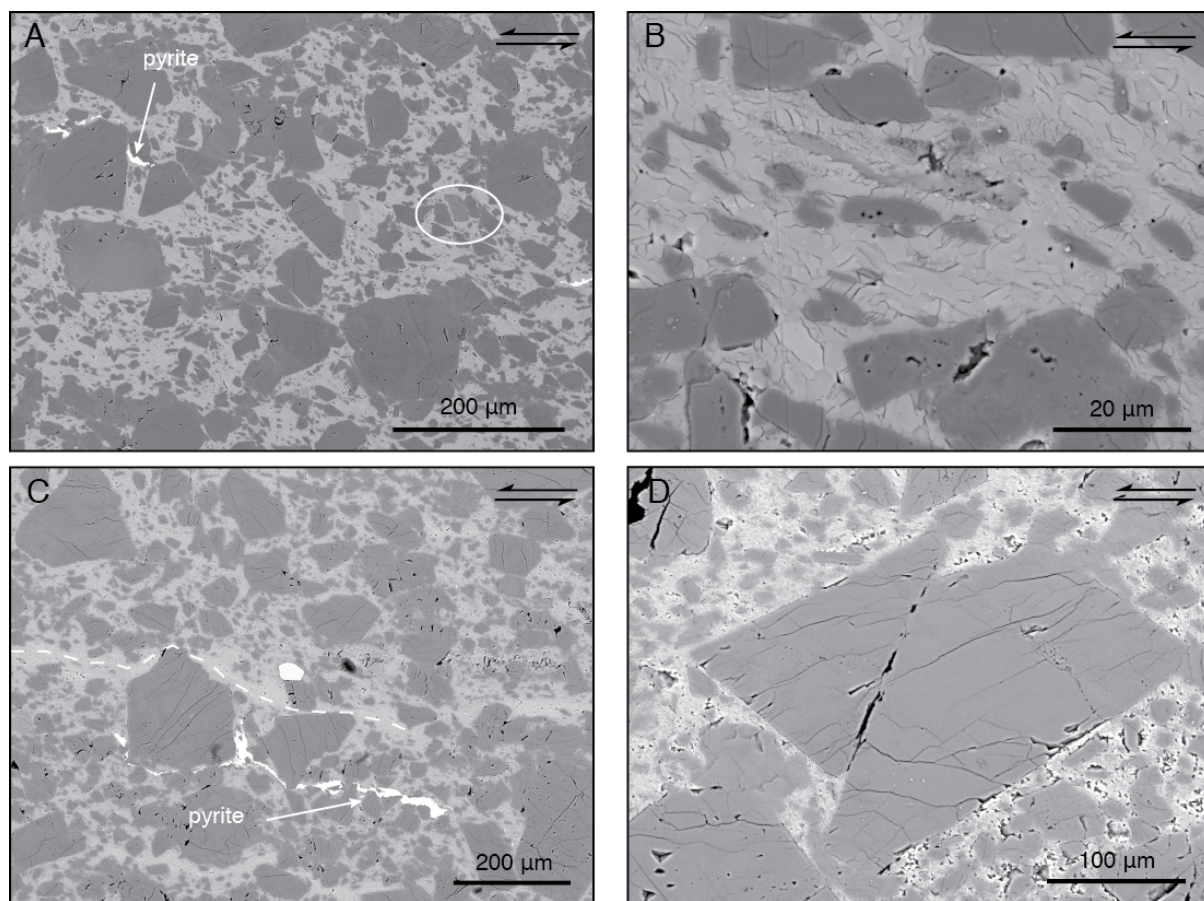




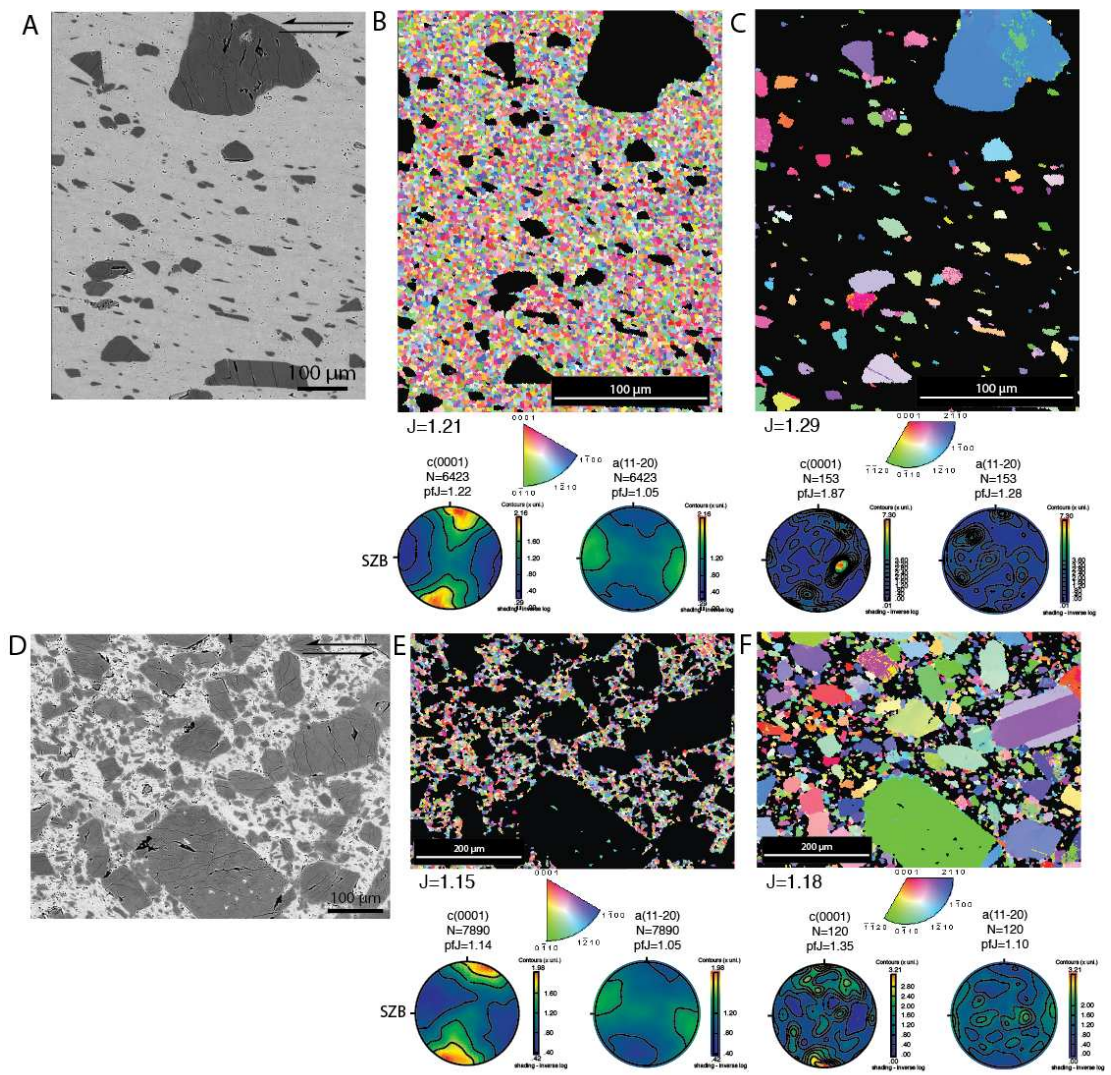
ACCEPTED MANUSCRIPT

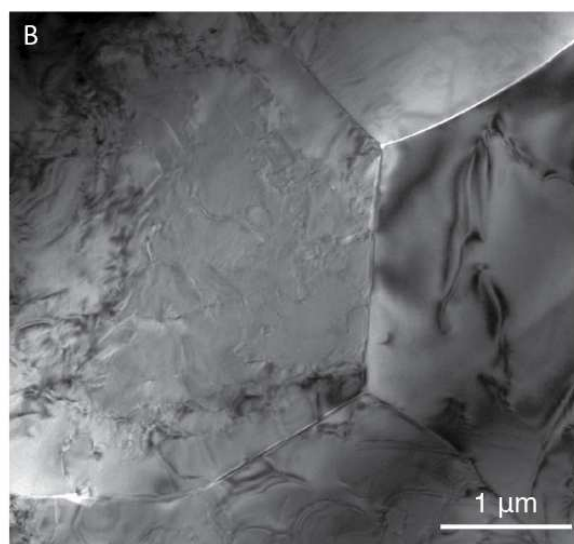
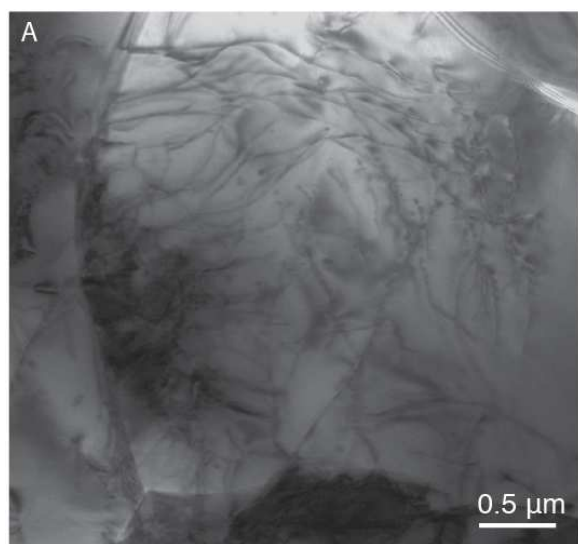




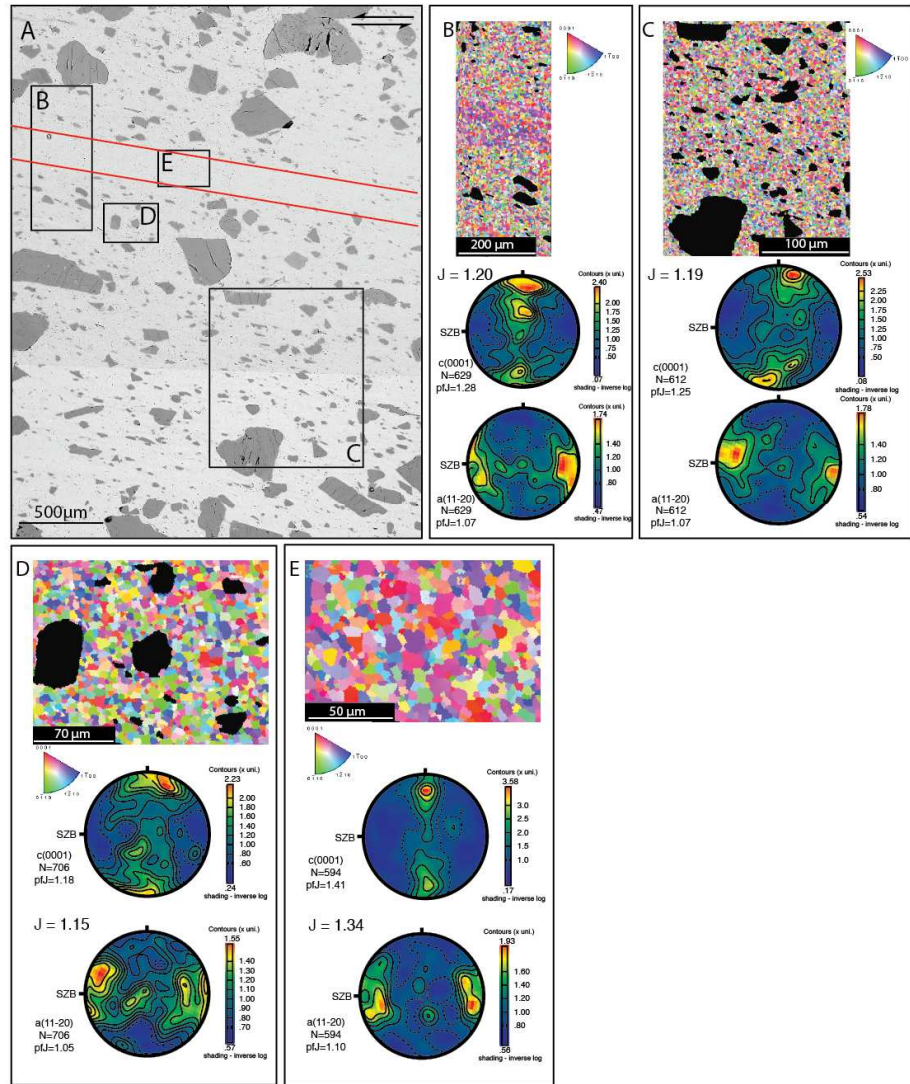


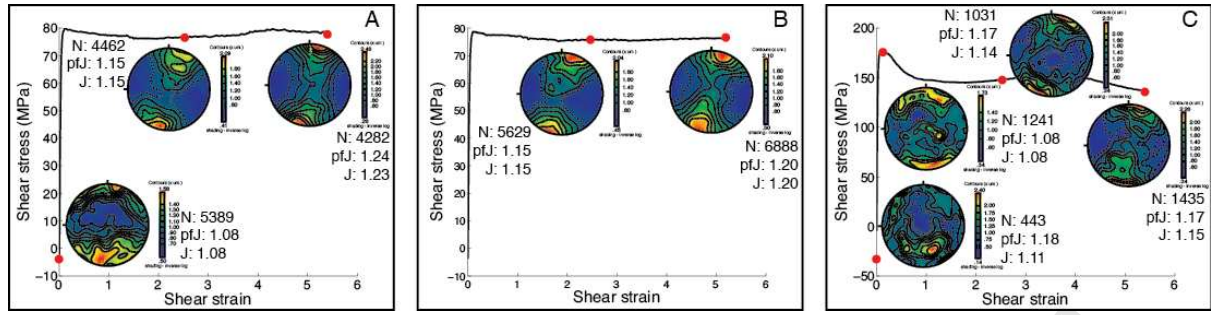
ACCEPTED

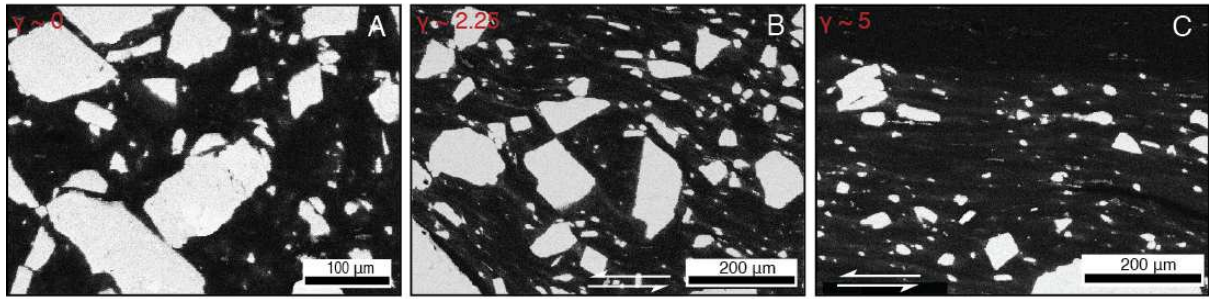




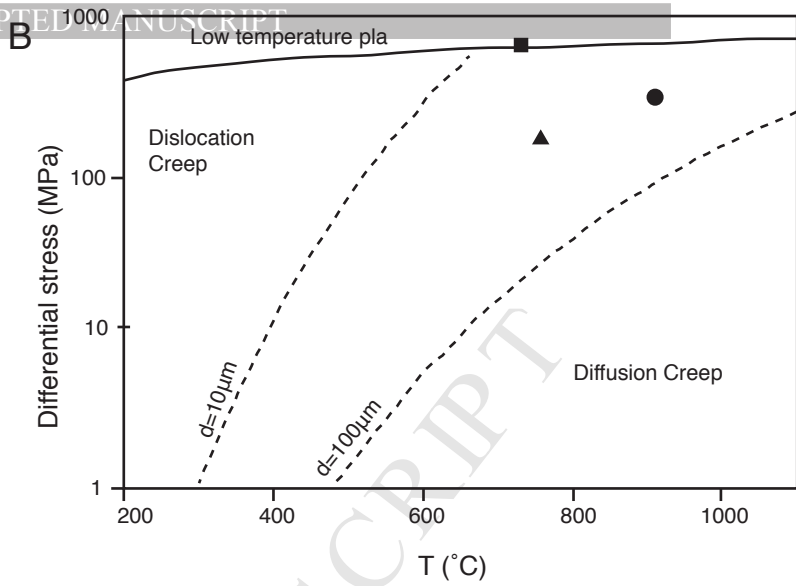
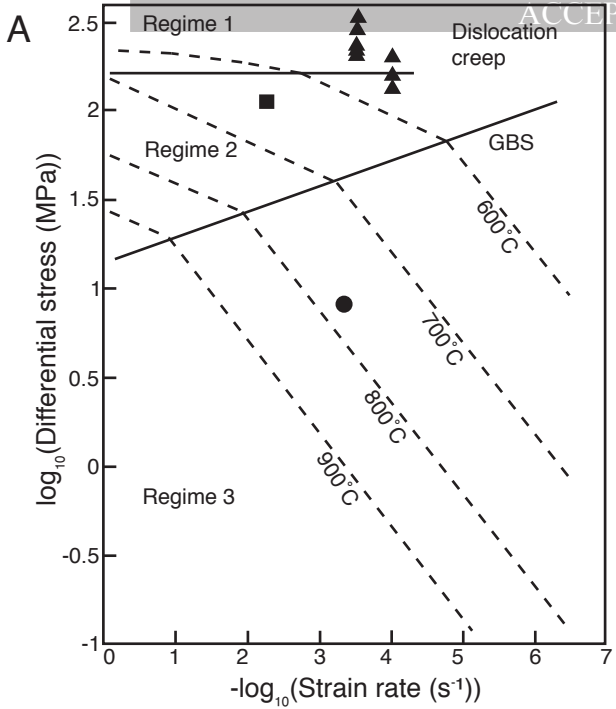
ACCEPTED MANUSCRIPT







ACCEPTED MANUSCRIPT



- The strength of calcite-dolomite composites increases with dolomite content.
- Calcite accommodates strain via grain boundary sliding accommodated by diffusion creep and limited dislocation creep.
- Dolomite leads to periodic embrittlement within the system, eventually allowing plastic flow of calcite.
- Grain boundary sliding is associated with CPO development.
- Monomineralic calcite bands accommodate more strain than bi-mineralic regions.

Supplementary Material – Microprobe Analysis

Microprobe analysis was performed on Dm25 and Dm75 deformed to high strain at 750°C (experiments P1527 and P1538). Figure S.1 is a map of all data points collected. Table S.1 gives xCa and xMg values at each point.

Figure S.1. Microprobe analysis maps. Data from Table S.1 is plotted as follows: yellow points represent Cc ($0.90 < x_{Ca} < 1.00$); green points represent Dm ($0.50 < x_{Ca} < 0.55$); red points represent Mg-enriched calcite ($0.55 < x_{Ca} < 0.90$). A. Microprobe analysis map for Dm25, P1527. B. Microprobe analysis map for Dm75, P1538.

Measurement Point	anion CO ₂	anion MgO	anion CaO	anion MnO	anion FeO	sum of x-site cation	xCa	xMg
'P1527_1_Scan3_1'	3.9768	0.1	1.9074	0.0027	0.0015	2.0116	0.9482	0.0497
'P1527_1_Scan3_2'	4.0527	0.4492	1.5184	0.0005	0.0056	1.9737	0.7693	0.2276
'P1527_1_Scan3_3'	4.0919	0.9298	1.0071	0.0012	0.0159	1.954	0.5154	0.4758
'P1527_1_Scan3_4'	4.0552	0.9527	1.0045	0.0013	0.0139	1.9724	0.5093	0.483
'P1527_1_Scan3_5'	4.048	0.0934	1.8816	0	0.001	1.976	0.9522	0.0472
'P1527_1_Scan3_6'	4.0326	0.1243	1.8564	0	0.0031	1.9837	0.9358	0.0627
'P1527_1_Scan3_7'	3.9979	0.1025	1.8959	0.0007	0.002	2.001	0.9474	0.0512
'P1527_1_Scan3_8'	4.0148	0.5163	1.4735	0.0002	0.0026	1.9926	0.7395	0.2591
'P1527_1_Scan3_9'	4.0552	0.0909	1.8771	0.002	0.0023	1.9724	0.9517	0.0461
'P1527_1_Scan3_10'	4.003	0.16	1.8335	0.0007	0.0043	1.9985	0.9174	0.0801
'P1527_1_Scan3_11'	4.0707	0.1161	1.8472	0	0.0013	1.9646	0.9402	0.0591
'P1527_1_Scan3_12'	3.9834	0.666	1.3355	0.0004	0.0064	2.0083	0.665	0.3316
'P1527_1_Scan3_13'	4.0165	0.5344	1.4495	0	0.0078	1.9917	0.7277	0.2683
'P1527_1_Scan3_14'	4.0305	0.9482	1.0176	0.0014	0.0175	1.9848	0.5127	0.4777
'P1527_1_Scan3_15'	4.04	0.9505	1.0105	0	0.019	1.98	0.5103	0.4801
'P1527_1_Scan3_16'	4.0309	0.121	1.8537	0	0.0099	1.9845	0.9341	0.0609
'P1527_1_Scan3_17'	4.0154	0.1114	1.8787	0.0005	0.0018	1.9923	0.943	0.0559
'P1527_1_Scan3_18'	4.1112	0.8974	1.0354	0.0008	0.0108	1.9444	0.5325	0.4615
'P1527_1_Scan3_19'	4.058	0.087	1.8828	0.0001	0.0011	1.971	0.9553	0.0442
'P1527_1_Scan3_20'	4.0394	0.7412	1.2265	0.0017	0.0109	1.9803	0.6193	0.3743
'P1527_1_Scan3_21'	4.0517	0.9514	1.0116	0.0014	0.0098	1.9742	0.5124	0.4819
'P1527_1_Scan3_22'	4.0916	0.1267	1.8251	0	0.0024	1.9542	0.9339	0.0648
'P1527_1_Scan3_23'	4.0508	0.0924	1.8812	0	0.001	1.9746	0.9527	0.0468
'P1527_1_Scan3_24'	4.0139	0.0698	1.9231	0.0001	0	1.9931	0.9649	0.035
'P1527_1_Scan3_25'	4.0043	0.0768	1.9209	0	0.0001	1.9978	0.9615	0.0385
'P1527_1_Scan3_26'	4.1012	0.9245	1.0035	0.0014	0.02	1.9494	0.5148	0.4742
'P1527_1_Scan3_27'	4.0163	0.9699	1.0104	0	0.0116	1.9919	0.5073	0.4869
'P1527_1_Scan3_28'	4.0299	0.1447	1.8372	0.0002	0.003	1.9851	0.9255	0.0729
'P1527_1_Scan3_29'	4.0392	0.8591	1.1071	0.0002	0.0141	1.9804	0.559	0.4338
'P1527_1_Scan3_30'	4.0826	0.0943	1.8626	0.0004	0.0015	1.9587	0.9509	0.0481
'P1527_1_Scan3_31'	4.0299	0.0824	1.9027	0	0	1.9851	0.9585	0.0415
'P1538_1_Scan4_1'	4.0297	0.9638	1.0036	0.0004	0.0174	1.9851	0.5056	0.4855
'P1538_1_Scan4_2'	4.0541	0.8177	1.1431	0.0002	0.012	1.9729	0.5794	0.4144
'P1538_1_Scan4_3'	4.0866	0.5664	1.3755	0.0014	0.0135	1.9567	0.703	0.2894
'P1538_1_Scan4_4'	4.052	0.9458	1.0066	0.0027	0.0189	1.974	0.5099	0.4791
'P1538_1_Scan4_5'	5.4704	1.0689	0.1651	0	0.0308	1.2648	0.1305	0.8451
'P1538_1_Scan4_6'	4.0593	0.8242	1.1338	0.0004	0.012	1.9704	0.5754	0.4183
'P1538_1_Scan4_7'	4.0453	0.4146	1.5548	0.0017	0.0064	1.9774	0.7863	0.2097
'P1538_1_Scan4_8'	5.3765	1.0137	0.2661	0	0.0319	1.3117	0.2029	0.7728
'P1538_1_Scan4_9'	4.0208	0.244	1.7439	0	0.0017	1.9896	0.8765	0.1226

Measurement Point	anion CO ₂	anion MgO	anion CaO	anion MnO	anion FeO	sum of x-site cation	xCa	xMg
'P1538_1_Scan4_10'	4.0303	0.2526	1.7291	0	0.0031	1.9848	0.8712	0.1273
'P1538_1_Scan4_11'	3.9954	0.6116	1.3775	0	0.0132	2.0023	0.688	0.3054
'P1538_1_Scan4_12'	4.005	0.954	1.0225	0	0.0209	1.9975	0.5119	0.4776
'P1538_1_Scan4_13'	4.0703	0.3188	1.6397	0.0003	0.0061	1.9649	0.8345	0.1623
'P1538_1_Scan4_14'	3.9921	0.2485	1.7506	0	0.0049	2.004	0.8736	0.124
'P1538_1_Scan4_15'	5.3297	1	0.3035	0.0004	0.0313	1.3351	0.2273	0.749
'P1538_1_Scan4_16'	4.0275	0.2997	1.6831	0.0004	0.0031	1.9863	0.8474	0.1509
'P1538_1_Scan4_17'	4.0487	0.2886	1.683	0.0001	0.004	1.9757	0.8519	0.1461
'P1538_1_Scan4_18'	4.0191	0.8969	1.0764	0.0023	0.0149	1.9905	0.5408	0.4506
'P1538_1_Scan4_19'	4.0512	0.2244	1.744	0	0.006	1.9744	0.8833	0.1136
'P1538_1_Scan4_20'	4.0398	0.2275	1.7464	0	0.0062	1.9801	0.882	0.1149
'P1538_1_Scan4_21'	4.0644	0.9409	1.0083	0.0006	0.018	1.9678	0.5124	0.4781
'P1538_1_Scan4_22'	4.0083	0.9745	1.0127	0	0.0087	1.9959	0.5074	0.4882
'P1538_1_Scan4_23'	4.0366	0.8325	1.1393	0.0012	0.0086	1.9817	0.5749	0.4201
'P1538_1_Scan4_24'	3.9877	0.5287	1.4693	0.0016	0.0066	2.0061	0.7324	0.2635
'P1538_1_Scan4_25'	4.051	0.3577	1.611	0	0.0058	1.9745	0.8159	0.1812
'P1538_1_Scan4_26'	4.0422	0.958	1.0063	0.0014	0.0132	1.9789	0.5085	0.4841
'P1538_1_Scan4_27'	4.0321	0.9484	1.0224	0.0005	0.0126	1.9839	0.5153	0.478
'P1538_1_Scan4_28'	4.0206	0.3519	1.6311	0.0003	0.0065	1.9897	0.8198	0.1768
'P1538_1_Scan4_29'	4.0119	0.2797	1.7101	0	0.0042	1.994	0.8576	0.1403
'P1538_1_Scan4_30'	4.0343	0.3951	1.5802	0.0005	0.0071	1.9829	0.7969	0.1992
'P1538_1_Scan4_31'	4.0021	0.5661	1.4204	0	0.0124	1.9989	0.7106	0.2832
'P1538_1_Scan4_32'	4.0717	0.8993	1.0524	0	0.0125	1.9641	0.5358	0.4578
'P1538_1_Scan4_33'	4.0094	0.306	1.6804	0.0011	0.0077	1.9953	0.8422	0.1534
'P1538_1_Scan4_35'	4.063	0.9209	1.0279	0.0002	0.0195	1.9685	0.5222	0.4678
'P1538_1_Scan4_36'	4.0375	0.2436	1.7313	0.0002	0.0061	1.9812	0.8739	0.1229
'P1538_1_Scan4_37'	4.0097	0.2306	1.7608	0.0015	0.0022	1.9951	0.8826	0.1156
'P1538_1_Scan4_38'	3.9981	0.9458	1.0373	0.0004	0.0175	2.001	0.5184	0.4727
'P1538_1_Scan4_39'	4.006	0.797	1.1846	0.0008	0.0146	1.997	0.5932	0.3991
'P1538_1_Scan4_40'	3.9713	0.9674	1.0289	0.0019	0.0162	2.0144	0.5108	0.4803
'P1538_1_Scan4_41'	3.9748	0.9435	1.0524	0.0003	0.0165	2.0126	0.5229	0.4688
'P1538_1_Scan4_42'	4.0177	0.2656	1.7218	0	0.0038	1.9912	0.8647	0.1334
'P1538_1_Scan4_43'	4.0178	0.9636	1.0125	0.0008	0.0143	1.9911	0.5085	0.4839
'P1538_1_Scan4_44'	4.012	0.9644	1.0157	0.0008	0.0131	1.994	0.5094	0.4836
'P1538_1_Scan4_45'	4.0054	0.9189	1.0637	0.0012	0.0136	1.9973	0.5326	0.4601
'P1538_1_Scan4_46'	4.0048	0.9705	1.0132	0.0006	0.0133	1.9976	0.5072	0.4858
'P1538_1_Scan4_47'	4.0462	0.9375	1.0264	0.0017	0.0113	1.9769	0.5192	0.4742
'P1538_1_Scan4_48'	3.9847	0.9823	1.01	0	0.0154	2.0077	0.5031	0.4893
'P1538_1_Scan4_49'	4.0671	0.2927	1.6676	0	0.0062	1.9665	0.848	0.1488
'P1538_1_Scan4_50'	4.0803	0.9191	1.0234	0.0009	0.0165	1.9599	0.5222	0.469

Measurement Point	anion CO2	anion MgO	anion CaO	anion MnO	anion FeO	sum of x-site cation	xCa	xMg
'P1538_1_Scan4_51'	3.9947	0.9127	1.0772	0.0002	0.0125	2.0027	0.5379	0.4558
'P1538_1_Scan4_52'	4.0099	0.2625	1.7285	0	0.004	1.9951	0.8664	0.1316
'P1538_1_Scan4_53'	4.0202	0.9551	1.018	0.0018	0.015	1.9899	0.5116	0.48
'P1538_1_Scan4_54'	4.026	0.7788	1.196	0.0005	0.0116	1.987	0.6019	0.3919
'P1538_1_Scan4_55'	4.0276	0.2161	1.7636	0.0006	0.0059	1.9862	0.8879	0.1088
'P1538_1_Scan4_56'	3.9652	0.7217	1.2812	0.0015	0.013	2.0174	0.6351	0.3577
'P1538_1_Scan4_57'	4.0506	0.2421	1.7277	0	0.0049	1.9747	0.8749	0.1226

